Research Article

Shabbir Ahmad, Moin-ud-Din Junjua*, Yashar Aryanfar, Adham E. Ragab, Ahmed S. Hendy, Jorge Luis Garcia Alcaraz, Ali Keçebaş, Mohammad Arsalan Khan*, Mohammad Mursaleen*, and Manzoore Elahi M. Soudagar

A penta-hybrid approach for modeling the nanofluid flow in a spatially dependent magnetic field

Abstract: The penta-hybrid nanofluid is a nanofluid that contains five different types of nanoparticles. It can achieve higher heat transfer rates than conventional hybrid nanofluids due to the synergistic effects of the nanoparticles. It also has more diverse physical and thermal properties, which make it more adaptable for various applications. Therefore, this research examines the influence of localized magnetic fields on the vortex dynamics in a penta-hybrid nanofluidic flow in a vertical cavity with an aspect ratio of 1:10, driven by a top and bottom lid moving in the opposite direction. The stream-vorticity formulation is used to solve the dimensionless governing partial differential equation. A confined magnetic field in the form of horizontal and vertical strips has been applied instead of a uniform magnetic field throughout the flow domain, which is more realistic. Moreover, MATLAB codes developed by the authors are used to investigate how these parameters affect the flow and thermal properties of the nanofluids. The results suggest that magnetic fields have an impact on how stress, flow patterns, and temperature are distributed. Moreover, the presence of a magnetic field influences the spacing of isotherms, indicating a more even temperature distribution. It has also been observed that stress distribution is affected by the magnetic field, with higher stress levels near walls and regions with velocity-induced stress. However, in certain areas, the magnetic field can decrease shear stress depending on its strength and orientation. These study findings have implications for designing and operating nanofluidic devices. For instance, utilizing a magnetic field can help regulate flow patterns, temperature distribution, and stress distribution within nanofluidic channels. This capability could prove beneficial for a range of applications, such as cell separation, drug delivery, and nanofluidic heat exchange systems.

* **Corresponding author: Moin-ud-Din Junjua,** School of Mathematical Sciences, Zhejiang Normal University, Jinhua, Zhejiang, 321004, China; Department of Mathematics, Ghazi University, Dera Ghazi Khan, 32200, Pakistan, e-mail: moinuddin@zjnu.edu.cn

* **Corresponding author: Mohammad Arsalan Khan,** Department of Civil Engineering, Zakir Husain College of Engineering and Technology, Aligarh Muslim University, Aligarh 202001, India; Geomechanics and Geotechnics Group, Kiel University, 24118, Kiel, Germany; New Era and Development in Civil Engineering Research Group, Scientific Research Center, Al-Ayen University, Thi-Qar, Nasiriyah, 64001, Iraq, e-mail: arsalan.khan@ifg.uni-kiel.de

* **Corresponding author: Mohammad Mursaleen,** China Medical University Hospital, China Medical University (Taiwan), Taichung 40402, Taiwan, e-mail: mursaleenm@gmail.com

Shabbir Ahmad: Graduate Program of Ocean Engineering, School of Engineering, Universidade Federal do Rio Grande, Italia Avenue, km 8, 96201-900, Rio Grande, Brazil; Department of Basic Sciences and Humanities, Muhammad Nawaz Sharif University of Engineering and Technology, Multan, 60000, Pakistan; Institute of Geophysics and Geomatics, China University of Geosciences, Wuhan, 430074, China

Yashar Aryanfar: The National Key Laboratory of Water Disaster Prevention, Hohai University, Hohai University, Nanjing, Jiangsu 211100, China; Department of Electric Engineering and Computation, Autonomous University of Ciudad Juárez. Av. Del Charro 450 Norte. Col. Partido Romero, Ciudad Juárez, 32310, Chihuahua, Mexico; Thermo-Fluids Research Group, Khazar University, Baku, AZ, Azerbaijan

Adham E. Ragab: Department of Industrial Engineering, College of Engineering, King Saud University, P.O. Box 800, Riyadh, 11421, Saudi Arabia

Ahmed S. Hendy: Department of Computational Mathematics and Computer Science, Institute of Natural Sciences and Mathematics, Ural Federal University, 19 Mira St, Yekaterinburg, 620002, Russia; Department of Mechanics and Mathematics, Western Caspian University, Baku, 1001, Azerbaijan

Jorge Luis Garcia Alcaraz: Department of Industrial and Manufacturing Engineering, Autonomous University of Ciudad Juárez. Av. Del Charro 450 Norte. Col. Partido Romero, Ciudad Juárez, 32310, Chihuahua, México

Ali Keçebaş: Department of Energy Systems Engineering, Technology Faculty, Muğla Sıtkı Koçman University, 48000, Menteşe, Muğla

Manzoore Elahi M. Soudagar: Centre of Research Impact and Outcome, Chitkara University, Rajpura, 140417, Punjab, India; Division of Research and Development, Lovely Professional University, Phagwara, Punjab, India

Nomenclature

Re	Reynolds number
V_0	constant velocity (m/s)
Ec	Eckert number
$\partial\tilde{H}/\partial x$	magnetic force components along the X-axis (T)
Mn	magnetic number
$\tilde{H}(x, y)$	magnetic field intensity (T)
κ	pyro magnetic factor (cm^2 K)
$\bar{T}_c$	Curie temperature (K)
$\partial\tilde{H}/\partial y$	magnetic force components along the Y-axis (T)
Pr	Prandtl number
$\tilde{M}$	magnetization property (A m^{-1})

Greek symbols

$\widehat{\rho_{nf}}$	density of nanofluid (kg m^{-3})
ε	dimensionless number
$\mu_{\text{pen-hnf}}$	viscosity of penta-hybrid nanofluid (Pa s)
$\widehat{\varphi_1}$	volume fraction of silver
$\widehat{\varphi_3}$	volume fraction of titanium dioxide
$\widehat{\varphi_5}$	volume fraction of iron(II, III) oxide
$\bar{\mu}_0$	magnetic permeability (H m^{-1})
$\sigma_{\text{pen-hnf}}$	electrical conductivity of penta-hybrid nanofluid (S/m)
$k_{\text{pen-hnf}}$	thermal conductivity of penta-hybrid nanofluid (W m^{-1} K^{-1})
$\widehat{\varphi_2}$	volume fraction of SWCNT
$\widehat{\varphi_4}$	volume fraction of copper
$\widehat{\rho}_{\text{pen-hnf}}$	density of nanofluid of penta-hybrid nanofluid (kg m^{-3})

1 Introduction

The importance of a lid-driven cavity lies in its capacity to depict various fluid flow phenomena, making it relevant to numerous engineering and scientific investigations. Lid-driven cavities provide insights into intricate fluid dynamics, including the formation of boundary layers, shedding of vortices, and separation of flows, acting as simplified models for comprehending these phenomena. They are widely used in computational fluid dynamics (CFD) research to validate numerical techniques, study turbulence modeling, and explore heat transfer processes. Moreover, lid-driven cavities have practical applications in diverse engineering domains like microfluidics, heat exchangers, and chemical processing due to their ability to replicate controlled flow conditions relevant to these fields. For example, Ismael *et al.* [1] explored Cu Al$_2$O$_3$ water hybrid nanofluids in a lid-driven cavity that was isothermally cooled by a triangular solid vertical wall with the aim of reducing the quantity of high thermal conductivity nanoparticles to enhance the method's cost-effectiveness. Ahlawat *et al.* [2] numerically investigated heat convection and entropy generation in a porous hexagonal cavity with a heated obstacle under a static magnetic field using a micropolar hybrid nanofluid composed of TiO$_2$ and graphene oxide in a water base. Rehman *et al.* [3] computationally analyzed nanoparticle flow in blood (modeled as a Carreau fluid) within a divergent/convergent channel, considering a nanofluid mixture of iron oxide and blood. Zhang *et al.* [4] used CFD to analyze cavitation flow in a reactor, evaluating rotor performance under various conditions and studying pressure pulsation time frequency. Waseem *et al.* [5] investigated hybrid Cu–MoS$_2$/water nanofluid flow over a nonlinearly stretched surface, noting increased skin friction with a higher stretching rate ratio and power index, but an inverse relationship with the Nusselt number (Nu). Idris *et al.* [6] utilized the finite-difference method to simulate fluid dynamics within a triangular lid-driven cavity by employing a vorticity formulation based on a stream function to explain their methodology. The accuracy and reliability of their simulations were evaluated through a comparative analysis with outcomes derived from the lattice Boltzmann method – a widely used computational tool in fluid dynamics. Khan *et al.* [7] developed a fractional model for the thermal flow of a hybrid nanofluid on an inclined surface, showing significant heat enhancement with water-based MoS$_2$ and graphene oxide nanomaterials compared to kerosene-based counterparts. Thirumalaisamy *et al.* [8] explored heat transmission properties in fluid flow within a square enclosure, studying the heat conduction of two hybrid nanofluids and observing significant variations in temperature and fluid flow parameters with changing Hartmann numbers and nanoparticle concentrations. Akram *et al.* [9] explored the free convection of Cu–water nanofluid in a hexagonal cavity with a square obstacle, examining how Rayleigh number, obstacle position, and nanoparticle volume fraction affect thermal behavior. Asghar *et al.* [10] examined slip effects in magnetized radiative ferrofluid flow, showing that increased velocity slip reduced heat transfer, while thermal slip and radiation increased the thermal boundary layer thickness. Li *et al.* [11] proposed a cavity magnomechanical system for transferring bipartite and tripartite entanglements, providing flexible control for potential quantum interfaces.

Nanofluids, comprising nanoparticles suspended in a base fluid like water, are a captivating subject within fluid dynamics due to their ability to enhance fluid properties. Hwang et al. [12] conducted experiments simulating a turbine blade cooling circuit, utilizing a triangular duct with tangential jets, and observed improved heat transfer efficiency with increasing Reynolds number. Waqas et al. [13] studied the melting of paraffin wax with hybrid nanomaterials (GO, SWCNTs) in a thermal energy storage (TES) unit, focusing on sustainable systems with varying nanoparticle concentrations. Hayat et al. [14] examined heat transfer over a radially stretched surface with Cu nanoparticles in water and silicone oil, transforming momentum and energy equations into nonlinear ordinary differential equations using similarity transformation. Hanif et al. [15] conducted research analyzing the unsteady Maxwell nanofluid model, incorporating a time derivative. The addition of the Cattaneo heat-flux to the energy equation enhanced the originality of the research. Shahzad et al. [16] analyzed the effect of surface residual stress on the nonlinear stability of perfect and imperfect cylindrical nanoscale shells under axial compression using a 3D shell model based on Gurtin–Murdoch elasticity theory. Hanif [17] investigated the mass and heat transport properties by the utilization of the implicit finite-difference method with MATLAB software to numerically solve a constructed mathematical model, examining various parameters' effects on associated distributions and graphically illustrating the results. Their findings indicate an increase in nanofluid velocity and temperature in the presence of heat generation. Additionally, at a 3% volume concentration of nanoparticles, the thermal conductivity of GO/kerosene exceeds that of CuO/kerosene, Al_2O_3/kerosene, TiO_2/kerosene, and Fe_3O_4/kerosene by 0.633, 0.443, 0.126, and 0.063%, respectively. Lone et al. [18] provided numerical solutions for MHD flow and heat/mass transfer over a stretching sheet in a hybrid nanofluid, using graphene oxide and silver nanoparticles suspended in kerosene. Li et al. [19] studied trihybrid nanoparticles in a cross-fluid model on a rotating stretched surface, considering heat sources, radiation, and convection effects. Rahman et al. [20] numerically explored heat exchange properties in a closed cavity, focusing on the impact of thermal conduction and magnetic fields, revealing a proportional decrease in average Nu with increasing Rayleigh numbers under electrical heating effects, and identifying magnetic flux as an effective control parameter for heat transportation and fluid velocity regulation. Selimefendigil et al. [21] employed computational techniques to investigate mixed convection in an enclosure, observing decreased heat transmission with higher Richardson and Hartmann numbers, but enhanced heat transfer performance with CuO nanoparticles at smaller Hartmann numbers. Lone et al. [22] studied ternary

hybrid nanofluid flow over an extending curved surface with TiO_2, $CoFe_2O_4$, and MgO nanoparticles in water, finding energy transfer rates increased by 17.31% (TiO_2–water) and 31.72% (TiO_2–$CoFe_2O_4$–water) as nanoparticle concentration rose. Żebrowska et al. [23] synthesized PDA nanoparticles coated with polyamidoamine dendrimers (DD3.0) for combined drug delivery, gene silencing, and photothermal therapy for glioblastoma multiforme, analyzing their physicochemical, photothermal, and cytotoxic properties. Korei and Benissaad [24] studied temperature and flow phenomena in a lid-driven cavity using a hybrid Al_2O_3–Cu/water nanofluid, noting decreased reversibility with smaller rounded corners, increased irreversibility with heightened heat conduction and viscosity, and suppressed entropy generation by increasing Hartmann numbers. Yasmin et al. [25] studied energy and mass transfer in Ag–Au hybrid nanofluid under heat source/sink effects using ethylene glycol as the base fluid.

The term "localized magnetic fields" refers to magnetic fields that demonstrate confinement within specific regions or areas. In contrast to the uniformity of magnetic fields, localized magnetic fields possess distinct characteristics of concentration and focus within specific regions. These fields can be produced using different methods such as the use of permanent magnets, electromagnets, or induced magnetic fields. There is a wide range of applications for localized magnetic fields, including magnetic sensors, magnetic recording, magnetic resonance imaging, magnetic hyperthermia, magnetic manipulation, etc. Researchers have developed new methods and gadgets to precisely regulate magnetic characteristics by altering magnetic fields locally. This topic is of great interest to the scientific community due to its importance and applicability. In this context, Panda et al. [26] explored heat transfer in Ag–MoS_4 hybrid nanofluid with variable magnetism, incorporating the Yamada–Ota model to account for viscous dissipation and heat sources. The study showed improved heat transfer efficiency compared to conventional fluids. Hanif [27] investigated unsteady flow and heat transfer of a viscoelastic fluid along a vertical plate, incorporating Friedrich shear stress, Cattaneo heat flux, and an external magnetic field. They developed a numerical solution method. Al-Kouz et al. [28] investigated heat transport in blood arteries using non-Newtonian hybrid nanofluids, focusing on magnetic forces, thermal radiation, and Joule heating. Increased thermal radiation raised blood temperature, while magnetic forces reduced velocity. Manna and Biswas [29] introduced a novel visualization tool that facilitates the examination of localized effects of varying magnetic force in the context of MHD convection within three distinct thermal cavities. The research findings suggest that the magnetic force at a particular location is impressive by the surrounding flow fields. Algehyne et al. [30] explored hybrid nanofluid (Cu/Al_2O_3–water) flow in a porous cavity, relevant for TES, with a perpendicular

magnetic field affecting fluid motion. By examining the effect of localized magnetic fields and flow characteristics of a hybrid nanofluid, Ali *et al.* [31] discovered that magnetic fields disturb nearby vortices and strengthen flow patterns, influencing heat transport more than skin friction. Hussain *et al.* [32] examined copper nanoparticle–water nanofluid flow in ducts, highlighting the importance of magnetic and thermal–hydraulic interactions in exhaust systems.

This study's novelty lies in several key aspects. First, it delves into the characteristics of a penta-hybrid nanofluid, a complex mixture containing five different types of nanoparticles that enhance both the thermal and magnetic properties of the fluid. Moreover, unlike traditional studies that usually focus on uniform magnetic fields, this research introduces a fresh approach by incorporating magnetic fields that vary spatially, offering a more realistic depiction of how magnetic fields are used in real-world applications. Furthermore, by using a lid-driven cavity, another unique element is introduced, allowing for an examination of how fluids behave in confined spaces when subjected to external forces. By exploring how these elements interact with each other, this study sheds light on uncharted territories within fluid dynamics and magnetic field interactions. The discoveries made here show great potential for advancements in areas like materials science, nanotechnology, and applications involving magnetic fluids. Essentially, this research significantly contributes to our knowledge about how multi-component nanofluids behave when exposed to spatially varying magnetic fields.

2 Problem description

In Figure 1, there is a detailed illustration of a vertical cavity with a unique aspect ratio of 1:10. This cavity contains a magnetic field integrated into the walls in the form of distinct strips, playing a significant role in the intriguing phenomena occurring inside. To comprehend the workings of this system, researchers utilize an advanced analytical tool known as the single-phase model (SPM). The SPM applies thermodynamic principles to delve into the complexities of the system. Central to the analysis is the formulation of stream vorticity, aiding in solving equations related to momentum, energy, and mass conservation. These equations are intricately presented within a two-dimensional Cartesian coordinate system, unveiling detailed patterns of heat transfer and fluid flow within this enclosed area.

2.1 Basic assumptions
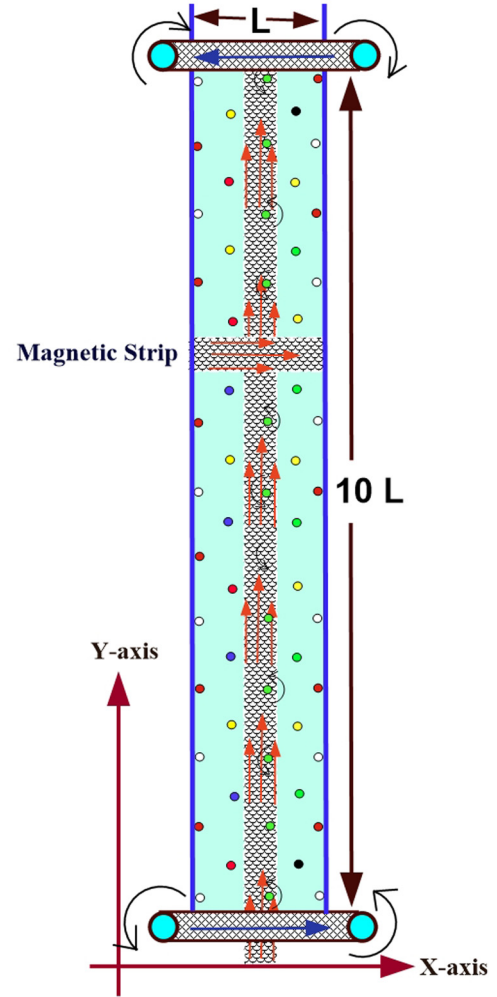
This study is based on the following assumptions:

Figure 1: Utilizing straight arrows to depict a magnetic field section in a diagram.

- The magnetic field intensity H generated by a magnetic source is defined as follows:

$$\tilde{H}_1(x, y) = H_0\{\tanh A'_1(x - x_1) - \tanh A'_2(x - x_2)\},$$
$$\tilde{H}_2(x, y) = H_0\{\tanh A'_1(y - y_1) - \tanh A'_2(y - y_2)\},$$

- A magnetic field is confined to a strip defined by $x_1 \leq x \leq x_2$; $0 \leq y \leq 10L$ and $y_1 \leq y \leq y_2$; $0 \leq x \leq L$, respectively.
- A vertical cavity has vertically insulated walls, while the horizontal walls are non-insulated and maintained at different temperatures. The top and bottom lids move in opposite directions.
- The fluid under investigation is a penta-hybrid nanofluid composed of solid nanostructures made of Ag, SWCNT, TiO_2, Cu, and Fe_3O_4.
- The thermophysical properties of the nanofluid, such as thermal conductivity, density, viscosity, and specific heat, remain constant throughout the study.

3 Mathematical formulation

The vector representation of the governing mathematical model is expressed as follows [33]:

$$
\left.\begin{array}{r}
\dfrac{\partial \rho_{\text{pen-hnf}}}{\partial t} + \nabla\cdot(\rho_{\text{pen-hnf}}\vec{V}) = 0, \\[2mm]
\rho_{\text{pen-hnf}}\left\{\dfrac{\partial}{\partial t}(\vec{V}) + \vec{V}\cdot(\vec{\nabla}\vec{V})\right\} = -\vec{\nabla}p + \mu_{\text{pen-hnf}}\nabla^2\vec{V} \\[2mm]
+ \rho_{\text{pen-hnf}}\vec{f}, \\[2mm]
(\rho c_p)_{\text{pen-hnf}}\left\{\dfrac{\partial}{\partial t}(T) + \vec{V}\cdot(\vec{\nabla}T)\right\} = k_{\text{pen-hnf}}\nabla^2 T \\[2mm]
+ \rho_{\text{pen-hnf}}F.
\end{array}\right\}. \quad (1)
$$

In dimensional notation, these equations can be written as follows [34]:

Continuity equation:

$$
\frac{\partial \tilde{U}}{\partial x} + \frac{\partial \tilde{V}}{\partial y} = 0, \quad (2)
$$

Momentum equation:

$$
\frac{\partial \tilde{U}}{\partial t'} + \left(\tilde{V}\frac{\partial \tilde{U}}{\partial y} + \tilde{U}\frac{\partial \tilde{U}}{\partial x}\right) = -\frac{1}{\widehat{\rho_{\text{pen-hnf}}}}\frac{\partial P}{\partial x}
$$
$$
+ \widehat{\upsilon_{\text{pen-hnf}}}\left(\frac{\partial^2 \tilde{U}}{\partial y^2} + \frac{\partial^2 \tilde{U}}{\partial x^2}\right) + \frac{\bar{\mu}_o\tilde{M}}{\widehat{\rho_{\text{pen-hnf}}}}\frac{\partial \tilde{H}}{\partial x}, \quad (3)
$$

$$
\frac{\partial \tilde{V}}{\partial t'} + \left(\tilde{U}\frac{\partial \tilde{V}}{\partial x} + \tilde{V}\frac{\partial \tilde{V}}{\partial y}\right) = -\frac{1}{\widehat{\rho_{\text{pen-hnf}}}}\frac{\partial P}{\partial y}
$$
$$
+ \widehat{\upsilon_{\text{pen-hnf}}}\left(\frac{\partial^2 \tilde{V}}{\partial x^2} + \frac{\partial^2 \tilde{V}}{\partial y^2}\right) + \frac{\bar{\mu}_o\tilde{M}}{\widehat{\rho_{\text{pen-hnf}}}}\frac{\partial \tilde{H}}{\partial y}. \quad (4)
$$

Energy equation [35]:

$$
\frac{(\widehat{\rho}\,c_p)_{\text{pen-hnf}}}{k_{\text{pen-hnf}}}\frac{\partial T}{\partial t'} + \frac{(\widehat{\rho}\,c_p)_{\text{pen-hnf}}}{k_{\text{pen-hnf}}}\left(\tilde{U}\frac{\partial T}{\partial x} + \tilde{V}\frac{\partial T}{\partial y}\right)
$$
$$
+ \left(\frac{\bar{\mu}_o}{k_{\text{pen-hnf}}}\right)T\frac{\partial \tilde{M}}{\partial T}\left(\tilde{V}\frac{\partial \tilde{H}}{\partial y} + \tilde{U}\frac{\partial \tilde{H}}{\partial x}\right) \quad (5)
$$
$$
= \nabla^2 T + \left(\frac{\tilde{\mu}_{\text{pen-hnf}}}{k_{\text{pen-hnf}}}\right)\left\{2\left(\frac{\partial \tilde{U}}{\partial x}\right)^2 + \left(\frac{\partial \tilde{V}}{\partial x} + \frac{\partial \tilde{U}}{\partial y}\right)^2 + 2\left(\frac{\partial \tilde{V}}{\partial y}\right)^2\right\}.
$$

Here,

Upon excluding the pressure component, we arrive at the following:

$$
\frac{\partial}{\partial t'}\left(\frac{\partial \tilde{U}}{\partial y} - \frac{\partial \tilde{V}}{\partial x}\right) + \widehat{V}\frac{\partial}{\partial y}\left(\frac{\partial \tilde{U}}{\partial y} - \frac{\partial \tilde{V}}{\partial x}\right) + \tilde{U}\frac{\partial}{\partial x}\left(\frac{\partial \tilde{U}}{\partial y} - \frac{\partial \tilde{V}}{\partial x}\right)
$$
$$
= \widehat{\upsilon_{\text{pen-hnf}}}\left(\frac{\partial^2}{\partial x^2} + \frac{\partial^2}{\partial y^2}\right)\left(\frac{\partial \tilde{U}}{\partial y} - \frac{\partial \tilde{V}}{\partial x}\right) + \left(\frac{\partial\left(\frac{\bar{\mu}_0\tilde{M}}{\widehat{\rho}_{\text{pen-hnf}}}\frac{\partial \tilde{H}}{\partial x}\right)}{\partial y} - \frac{\partial\left(\frac{\bar{\mu}_0\tilde{M}}{\widehat{\rho}_{\text{pen-hnf}}}\frac{\partial \tilde{H}}{\partial y}\right)}{\partial x}\right).
$$
$$
(6)
$$

3.1 Boundary conditions

For the existing problem, the dimensional boundary conditions are as follows:

Right and left vertical walls (adiabatic): Heat transfer is completely restricted across these walls,

$$
\left.\begin{array}{l}
\tilde{U}(0, y) = \tilde{U}(L, y) = 0, \quad \left(\dfrac{\partial T}{\partial x}\right)_{x=0} = \left(\dfrac{\partial T}{\partial x}\right)_{x=L} = 0, \\[2mm]
\tilde{V}(0, y) = \tilde{V}(L, y) = 0;
\end{array}\right\} \quad (7a)
$$

$$
0 < y < 10L
$$

Upper horizontal wall:

$$
\left.\begin{array}{l}
\tilde{U}(x, L) = -V_0, \quad T(x,\ L) = T_c, \\[2mm]
\tilde{V}(x, L) = 0;
\end{array}\right\} \quad 0 < x < L \quad (7b)
$$

Lower horizontal wall:

$$
\left.\begin{array}{l}
\tilde{U}(x, 0) = V_0, \quad T(x, 0) = T_h \\[2mm]
\tilde{V}(x, 0) = 0;
\end{array}\right\} \quad 0 < x < L. \quad (7c)
$$

3.2 Thermophysical properties of Ag–SWCNT–TiO$_2$–Cu–Fe$_3$O$_4$–water-based penta-hybrid nanofluids and simple nanofluids

In this section, we outline the thermophysical properties of the penta-hybrid nanofluids utilized in our analysis, which

$\bar{\mu}_0\tilde{M}\frac{\partial \tilde{H}}{\partial x}$	Magnetic force components along the x-axis
$\bar{\mu}_0 T\frac{\partial \tilde{M}}{\partial T}\left(\tilde{U}\frac{\partial \tilde{H}}{\partial x} + \tilde{V}\frac{\partial \tilde{H}}{\partial y}\right)$	Magneto-caloric phenomenon
$\tilde{M} = K\tilde{H}(\bar{T}_c - T).$	Magnetization property
$\bar{\mu}_0\tilde{M}\frac{\partial \tilde{H}}{\partial y}$	Magnetic force components along the y-axis
$\frac{\partial^2 \tilde{U}}{\partial y^2} + \frac{\partial^2 \tilde{U}}{\partial x^2}$	Diffusion terms
$\bar{T}_c$	Curie temperature [35]

are crucial for investigating the heat transport problem. We adopt a specific set of thermophysical properties for the penta-hybrid nanofluids composed of Ag–SWCNT–TiO$_2$–Cu–Fe$_3$O$_4$ nanoparticles. These properties, including density, specific heat, thermal conductivity, and viscosity, are sourced from existing literature [36–38]. Table 1 illustrates a comparison of the thermophysical properties of penta-hybrid nanofluids with conventional nanofluids.

For conducting the analysis, it is necessary to utilize these dimensionless variables [39]:

$$\xi = \frac{x}{L}, y = \frac{y}{L}, u = \frac{\tilde{U}}{V_0}, v = \frac{\tilde{V}}{V_0}, \widehat{\theta} = \frac{T - T_c}{\Delta T},$$
$$H = \frac{\tilde{H}}{H_0}, t = \frac{V_0}{L}t'. \tag{8}$$

	For penta-hybrid nanofluids	For nano-fluids	For base fluids (water)	For solid				
				Silver (s_1)	SWCNT (s_2)	Titanium dioxide (s_3)	Copper (s_4)	Iron oxide (s_5)
Density	$\widehat{\rho}_{\text{pen-hnf}}$	$\widehat{\rho}_{\text{nf}}$		$\widehat{\rho}_{s1}$	$\widehat{\rho}_{s2}$	$\widehat{\rho}_{s3}$	$\widehat{\rho}_{s4}$	$\widehat{\rho}_{s5}$
Electrical conductivity	$\sigma_{\text{pen-hnf}}$	σ_{nf}	σ_{bf}	σ_{s1}	σ_{s2}	σ_{s3}	σ_{s4}	σ_{s5}
Thermal conductivity	$k_{\text{pen-hnf}}$	k_{nf}	k_{bf}	k_{s1}	k_{s2}	k_{s3}	k_{s4}	k_{s5}
Nanoparticles volume fraction				$\widehat{\varphi}_1$	$\widehat{\varphi}_2$	$\widehat{\varphi}_3$	$\widehat{\varphi}_4$	$\widehat{\varphi}_5$
Viscosity	$\mu_{\text{pen-hnf}}$	μ_{nf}	μ_f					

The formulas found in existing literature can be used to calculate the thermal and physical properties of both nanofluids and hybrid nanofluids.

We can infer from equations (4) and (5) that

Table 1: Comparative thermophysical analysis of penta-hybrid nanofluids and traditional nanofluids

Properties	Penta-hybrid nanofluid
Density	$\widehat{\rho}_{\text{pen-hnf}} = (1-\widehat{\varphi}_5)\{(1-\widehat{\varphi}_4)((1-\widehat{\varphi}_3)[(1-\widehat{\varphi}_1)\{(1-\widehat{\varphi}_2)\widehat{\rho}_f + \widehat{\varphi}_1\widehat{\rho}_{s1}\} + \widehat{\varphi}_2\widehat{\rho}_{s2}]$ $+ \widehat{\varphi}_3\widehat{\rho}_{s3}) + \widehat{\varphi}_4\widehat{\rho}_{s4}\} + \widehat{\varphi}_5\widehat{\rho}_{s5}$
Heat capacity	$(\widehat{\rho} c_p)_{\text{pen-hnf}} = (1-\widehat{\varphi}_5)\left\{ \begin{matrix} (1-\widehat{\varphi}_4)((1-\widehat{\varphi}_3)[(1-\widehat{\varphi}_1)\{(1-\widehat{\varphi}_2)C_{pf}\widehat{\rho}_f + \widehat{\varphi}_1 C_{ps1}\widehat{\rho}_{s1}\} + \widehat{\varphi}_2 C_{ps2}\widehat{\rho}_{s2}] + \widehat{\varphi}_3 C_{ps3}\widehat{\rho}_{s3}) \\ + \widehat{\varphi}_4 C_{ps4}\widehat{\rho}_{s4} \end{matrix} \right\} + \widehat{\varphi}_5 C_{ps5}\widehat{\rho}_{s5}$
Viscosity	$\mu_{\text{pen-hnf}} = \frac{\mu_f}{(1-\widehat{\varphi}_1)^{2.5}(1-\widehat{\varphi}_2)^{2.5}(1-\widehat{\varphi}_3)^{2.5}(1-\widehat{\varphi}_4)^{2.5}(1-\widehat{\varphi}_5)^{2.5}}$
Thermal conductivity	$\frac{k_{\text{pen\_hnf}}}{k_{\text{tet\_hnf}}} = \frac{k_{s5} + (n-1)(k_{\text{tet\_hnf}} - (n-1)\widehat{\varphi}_{s5})(k_{\text{tet\_hnf}} - k_{s5})}{k_{s5} + (n-1)k_{\text{tet\_hnf}} + \widehat{\varphi}_{s5}(k_{\text{tet\_hnf}} - k_{s5})}$, $\frac{k_{\text{tet\_hnf}}}{k_{\text{thnf}}} = \frac{k_{s4} + (n-1)(k_{\text{thnf}} - (n-1)\widehat{\varphi}_{s4})(k_{\text{thnf}} - k_{s4})}{k_{s4} + (n-1)k_{\text{thnf}} + \widehat{\varphi}_{s4}(k_{\text{thnf}} - k_{s4})}$, $\frac{k_{\text{pen\_hnf}}}{k_{\text{tet\_hnf}}} = \frac{k_{s5}(n-1)(k_{\text{tet\_hnf}} - (n-1)\widehat{\varphi}_{s5})(k_{\text{tet\_hnf}} - k_{s5})}{k_{s5} + (n-1)k_{\text{tet\_hnf}} + \widehat{\varphi}_{s5}(k_{\text{tet\_hnf}} - k_{s5})}$, $\frac{k_{\text{tethnf}}}{k_{\text{thnf}}} = \frac{k_{s4} + (n-1)(k_{\text{thnf}} - (n-1)\widehat{\varphi}_{s4})(k_{\text{thnf}} - k_{s4})}{k_{s4} + (n-1)k_{\text{thnf}} + \widehat{\varphi}_{s4}(k_{\text{thnf}} - k_{s4})}$, $\frac{k_{\text{thnf}}}{k_{\text{hnf}}} = \frac{k_{s3} + (n-1)(k_{\text{hnf}} - (n-1)\widehat{\varphi}_{s3})(k_{\text{hnf}} - k_{s3})}{k_{s3} + (n-1)k_{\text{hnf}} + \widehat{\varphi}_{s3}(k_{\text{hnf}} - k_{s3})}$, where $\frac{k_{\text{hnf}}}{k_{\text{nf}}} = \frac{1-\widehat{\varphi}_2 + 2\widehat{\varphi}_2\frac{k_{s2}}{k_{s2}-k_{\text{nf}}}\ln\frac{k_{s2}+k_{\text{nf}}}{2k_{\text{nf}}}}{1-\widehat{\varphi}_2 + 2\widehat{\varphi}_2\frac{k_{\text{nf}}}{k_{s2}-k_{\text{nf}}}\ln\frac{k_{s2}+k_{\text{nf}}}{2k_{\text{nf}}}}$, and $\frac{k_{nf}}{k_f} = \frac{k_{s1} - (n-1)\widehat{\varphi}_1(k_f - k_{s1}) + (n-1)k_f}{k_{s1} + \widehat{\varphi}_1(k_f - k_{s1}) + (n-1)k_f}$.
Electric conductivity	$\frac{\sigma_{\text{pen\_hnf}}}{\sigma_{\text{tet\_hnf}}} = \frac{\sigma_{s5} - 2\widehat{\varphi}_5(\sigma_{\text{tet\_hnf}} - \sigma_{s5}) + 2\sigma_{\text{tet\_hnf}}}{\sigma_{s5} + \widehat{\varphi}_5(\sigma_{\text{tet\_hnf}} - \sigma_{s5}) + 2\sigma_{\text{tet\_hnf}}}$, $\frac{\sigma_{\text{tet\_hnf}}}{\sigma_{\text{thnf}}} = \frac{\sigma_{s4} - 2\widehat{\varphi}_4(\sigma_{\text{thnf}} - \sigma_{s4}) + 2\sigma_{\text{thnf}}}{\sigma_{s4} + \widehat{\varphi}_4(\sigma_{\text{thnf}} - \sigma_{s4}) + 2\sigma_{\text{thnf}}}$, $\frac{\sigma_{\text{thnf}}}{\sigma_{\text{hnf}}} = \frac{\sigma_{s3} - 2\widehat{\varphi}_3(\sigma_{\text{hnf}} - \sigma_{s3}) + 2\sigma_{\text{hnf}}}{\sigma_{s3} + \widehat{\varphi}_3(\sigma_{\text{hnf}} - \sigma_{s3}) + 2\sigma_{\text{hnf}}}$, where $\frac{\sigma_{\text{hnf}}}{\sigma_{nf}} = \frac{\sigma_{s2} - 2\widehat{\varphi}_2(\sigma_{nf} - \sigma_{s2}) + 2\sigma_{nf}}{\sigma_{s2} + \widehat{\varphi}_2(\sigma_{nf} - \sigma_{s2}) + 2\sigma_{nf}}$, and $\frac{\sigma_{nf}}{\sigma_f} = \frac{\sigma_{s1} - 2\widehat{\varphi}_1(\sigma_f - \sigma_{s1}) + 2\sigma_f}{\sigma_{s1} + \widehat{\varphi}_1(\sigma_f - \sigma_{s1}) + 2\sigma_f}$.

$$\frac{\partial J}{\partial t} + u\frac{\partial J}{\partial \xi} + v\frac{\partial J}{\partial \eta} = \left(\frac{\widehat{\rho}_{\text{pen\_hnf}}}{\widehat{\rho}_f}\right)\left(\frac{\mu_f}{\mu_{\text{pen\_hnf}}}\right)\frac{1}{\text{Re}}\nabla^2 J$$
$$+ \frac{Mn}{\left(\frac{\widehat{\rho}_{\text{pen\_hnf}}}{\widehat{\rho}_f}\right)}H\left(\frac{\partial H}{\partial \eta}\cdot\frac{\partial \widehat{\theta}}{\partial \xi} - \frac{\partial H}{\partial \xi}\cdot\frac{\partial \widehat{\theta}}{\partial \eta}\right), \quad (9)$$

$$\nabla^2\widehat{\theta} = \text{Pr}^*\left(\frac{\widehat{\rho}_{\text{pen\_hnf}}}{\widehat{\rho}_f}\right)\left(\frac{\mu_f}{\mu_{\text{pen\_hnf}}}\right)$$
$$\times \left(\frac{(\widehat{\rho}\,c_p)_{\text{pen\_hnf}}}{(\widehat{\rho}\,c_p)_f}\right)\text{Re}^*\left(\frac{1}{\left(\frac{\mu_f}{\mu_{\text{pen\_hnf}}}\right)\left(\frac{\widehat{\rho}_{\text{pen\_hnf}}}{\widehat{\rho}_f}\right)}\right)\left\{\frac{\partial\widehat{\theta}}{\partial\xi}\frac{\partial\tilde{\psi}}{\partial\eta}\right.$$
$$\left.- \frac{\partial\widehat{\theta}}{\partial\eta}\frac{\partial\tilde{\psi}}{\partial\xi}\right\} + \text{Pr}*\left(\frac{\mu_f}{\mu_{\text{pen\_hnf}}}\right)\left(\frac{\widehat{\rho}_{\text{pen\_hnf}}}{\widehat{\rho}_f}\right)$$
$$\times \left(\frac{(\widehat{\rho}\,c_p)_{\text{pen\_hnf}}}{(\widehat{\rho}\,c_p)_f}\right)\times\frac{Mn}{\left(\frac{\widehat{\rho}_{\text{pen\_hnf}}}{\widehat{\rho}_f}\right)}\text{Re} \qquad (10)$$
$$\times \left(\frac{1}{\left(\frac{\mu_f}{\mu_{\text{pen\_hnf}}}\right)\left(\frac{\widehat{\rho}_{\text{pen\_hnf}}}{\widehat{\rho}_f}\right)}\right)\text{Ec}H(\varepsilon - \tilde{\psi})\left\{\frac{\partial H}{\partial\xi}\frac{\partial\tilde{\psi}}{\partial\eta} - \frac{\partial H}{\partial\eta}\frac{\partial\tilde{\psi}}{\partial\xi}\right\}$$
$$+ \text{Pr}^*\left(\frac{\widehat{\rho}_{\text{pen\_hnf}}}{\widehat{\rho}_f}\right)\left(\frac{\mu_f}{\mu_{\text{pen\_hnf}}}\right)$$
$$\times \left(\frac{(\widehat{\rho}\,c_p)_{\text{pen\_hnf}}}{(\widehat{\rho}\,c_p)_f}\right)\text{Ec}\left\{\left(\frac{\partial^2\tilde{\psi}}{\partial\eta^2} - \frac{\partial^2\tilde{\psi}}{\partial\xi^2}\right)^2 + 4\left(\frac{\partial^2\tilde{\psi}}{\partial\xi\partial\eta}\right)^2\right\},$$

where

$$H_1(\xi, \eta) = H_0\{\tanh A_1(\xi - \xi_1) - \tanh A_2(\xi - \xi_2)\}$$
$$H_2(\xi, \eta) = H_0\{\tanh A_1(\eta - \eta_1) - \tanh A_2(\eta - \eta_2)\}, \qquad (11)$$

in the strips defined by $\xi_1 \leq \xi \leq \xi_2$; $0 \leq \eta \leq 10$ and $\eta_1 \leq \eta \leq \eta_2$; $0 \leq \xi \leq 1$, respectively.

Finally,

$$H(\xi, \eta) = H_1(\xi, \eta) + H_2(\xi, \eta). \qquad (12)$$

With the stream-vorticity formulation, equations (1)–(4) are modified to include

$$\widehat{u} = \frac{\partial\tilde{\psi}}{\partial\eta}, \quad \widehat{v} = \frac{\partial\tilde{\psi}}{\partial\xi} \text{ and}$$
$$\left(\frac{\partial\widehat{u}}{\partial\eta} - \frac{\partial\widehat{v}}{\partial\xi}\right) = -\widehat{\omega} \text{ or } \left\{\left(\frac{\partial^2\tilde{\psi}}{\partial\xi^2} + \frac{\partial^2\tilde{\psi}}{\partial\eta^2}\right) = -\widehat{\omega}\right\}. \qquad (13)$$

Similarly, the non-dimensional boundary conditions are

Left and right vertical walls (adiabatic):

$$\widehat{u}(0, \eta) = \widehat{u}(1, \eta) = 0, \quad \left.\left(\frac{\partial\theta}{\partial\xi}\right)\right|_{\xi=0} = 0, \left.\left(\frac{\partial\theta}{\partial\xi}\right)\right|_{\xi=1} = 0, \left.\right\}$$
$$\widehat{v}(0, \eta) = \widehat{v}(1, \eta) = 0, \qquad (14a)$$
$$0 < \eta < 10.$$

Upper horizontal wall:

$$\left.\begin{array}{l}\widehat{u}(\xi, 1) = -1, \quad \widehat{\theta}(\xi, 1) = 0,\\ \widehat{v}(\xi, 1) = 0;\end{array}\right\} \quad 0 < \xi < 1. \qquad (14b)$$

Lower horizontal wall:

$$\left.\begin{array}{l}\widehat{u}(\xi, 0) = 1, \quad \widehat{\theta}(\xi, 0) = 1,\\ v(\xi, 0) = 0;\end{array}\right\} \quad 0 < \xi < 1. \qquad (14c)$$

3.2.1 Physical quantities of interest

The key variables under examination in this study are the Nu and the skin friction coefficient (CfRe), which are defined as follows [40]:

$$\text{Nu} = \frac{\widehat{q}\,L}{k_{\text{pen\_hnf}}\Delta T} \text{ and } \text{CfRe} = \frac{2\tau}{\widehat{\rho}_{\text{pen\_hnf}}v_0{}^2}$$

where

$\tau = \tilde{\mu}_{\text{pen\_hnf}}\left(\frac{\partial\widehat{u}}{\partial\eta}\right)\Big|_{\eta=0,L}$	shear stress	$\widehat{q} = -k_{\text{pen\_hnf}}\left(\frac{\partial T}{\partial\eta}\right)\Big|_{\eta=0,L}$ Heat flux

The dimensionless parameters lead to the following outcomes:

$$\text{CfRe} = \left(\frac{\widehat{\rho}_f}{\widehat{\rho}_{\text{pen\_hnf}}}\right)\left(\frac{\mu_{\text{pen\_hnf}}}{\mu_f}\right)\frac{\partial\widehat{u}}{\partial y}, \quad \text{and } N_u = \left(\frac{k_{\text{pen\_hnf}}}{k_f}\right)\frac{\partial\widehat{\theta}}{\partial y}.$$

4 Alternating direction implicit (ADI) technique

To address equations (4), (5), and (6), which govern heat transfer and fluid flow within an enclosure, a numerical approach called ADI has been employed. This approach deals with the equations step by step, focusing on one direction while keeping the other constant. This method

improves both the speed and stability of finding solutions. It uses central differences to estimate changes at a point by averaging values from nearby points. By transforming equations into algebraic forms on a grid, this technique ensures accuracy throughout the process. The ADI method belongs to finite-difference methods, known for their flexibility in solving governing equations. Finite differences can handle abrupt data changes, making this method highly adaptable. The finite-difference method is valued for its simplicity and precision, which can be enhanced by including more points in the stencil. A collection of points is used to calculate changes at a specific point.

To move from time level n to time level $n + 1$, the procedure involves the following details:

$$
\frac{\widehat{w}_{i,j}^{\left(\frac{n+1}{2}\right)} - \widehat{w}_{i,j}^{(n)}}{\frac{\delta t}{2}} = \frac{1}{\mathrm{Re}} \left(\frac{1}{\left(\frac{\widehat{\rho}_{\mathrm{pen\_hnf}}}{\widehat{\rho}_f}\right)\left(\frac{\mu_f}{\mu_{\mathrm{pen\_hnf}}}\right)} \right) \times \left\{ \frac{\widehat{w}_{i-1,j}^{\left(\frac{n+1}{2}\right)} - 2\widehat{w}_{i,j}^{\left(\frac{n+1}{2}\right)} + \widehat{w}_{i+1,j}^{\left(\frac{n+1}{2}\right)}}{h^2} + \frac{\widehat{w}_{i,j-1}^{(n)} - 2\widehat{w}_{i,j}^{(n)} + \widehat{w}_{i,j+1}^{(n)}}{k^2} \right\}
$$

$$
+ \frac{\mathrm{Mn}}{\left(\frac{\widehat{\rho}_{\mathrm{pen\_hnf}}}{\widehat{\rho}_f}\right)} H_{i,j} \left[\frac{H_{i,j+1} - H_{i,j-1}}{2k} \frac{\widehat{\theta}_{i+1,j}^{(n)} - \widehat{\theta}_{i-1,j}^{(n)}}{2h} - \frac{H_{i+1,j} - H_{i-1,j}}{2h} \frac{\widehat{\theta}_{i,j+1}^{(n)} - \widehat{\theta}_{i,j-1}^{(n)}}{2k} \right] \tag{15}
$$

$$
- \widehat{u}_{i,j}^{\left(\frac{n+1}{2}\right)} \left(\frac{\widehat{w}_{i+1,j}^{(n+1)} - \widehat{w}_{i-1,j}^{(n+1)}}{2h} \right) - \widehat{v}_{i,j}^{\left(\frac{n+1}{2}\right)} \left(\frac{\widehat{w}_{i,j+1}^{(n)} - \widehat{w}_{i,j-1}^{(n)}}{2k} \right),
$$

$$
\frac{\widehat{\theta}_{i,j}^{(n+1/2)} - \widehat{\theta}_{i,j}^{(n)}}{\delta t/2} = \left\{ \frac{\widehat{\theta}_{i-1,j}^{(n+1/2)} - 2\widehat{\theta}_{i,j}^{(n+1/2)} + \widehat{\theta}_{i+1,j}^{(n+1/2)}}{h^2} + \frac{\widehat{\theta}_{i,j-1}^{(n)} + \widehat{\theta}_{i,j+1}^{(n)} - 2\widehat{\theta}_{i,j}^{(n)}}{k^2} \right\} + \mathrm{Pr} \times (\mu_f/\mu_{\mathrm{pen\_hnf}})(\widehat{\rho}_{\mathrm{pen\_hnf}}/\widehat{\rho}_f)
$$

$$
\times \left(\frac{(\widehat{\rho}\,c_{\mathrm{p}})_{\mathrm{pen\_hnf}}}{(\widehat{\rho}\,c_{\mathrm{p}})_f} \right) \times \frac{\mathrm{Mn}}{(\widehat{\rho}_{\mathrm{pen\_hnf}}/\widehat{\rho}_f)} \mathrm{Re} \times (\mu_{\mathrm{pen\_hnf}}/\mu_f)(\widehat{\rho}_f/\widehat{\rho}_{\mathrm{pen\_hnf}}) H_{i,j}(\tilde{\psi}_{i,j} - \varepsilon) \left[\widehat{u}_{i,j}^{(n+1/2)} \frac{H_{i,j+1} - H_{i,j-1}}{2k} \right.
$$

$$
\left. + \widehat{v}_{i,j}^{(n+1/2)} \frac{H_{i+1,j} - H_{i-1,j}}{2h} \right] - \widehat{u}_{i,j}^{(n+1/2)} \left(\frac{\widehat{\theta}_{i+1,j}^{(n+1/2)} - \widehat{\theta}_{i-1,j}^{(n+1/2)}}{2h} \right) - \widehat{v}_{i,j}^{(n+1/2)} \left(\frac{\widehat{\theta}_{i,j+1}^{(n)} - \widehat{\theta}_{i,j-1}^{(n)}}{2k} \right) - \mathrm{Pr} \tag{16}
$$

$$
\times \left(\frac{(\widehat{\rho}_{\mathrm{pen\_hnf}}/\widehat{\rho}_f)}{(1 - \widehat{\varphi}_1)^{-2.5}(1 - \widehat{\varphi}_2)^{-2.5}} \right) (\mu_f/\mu_{\mathrm{pen\_hnf}})
$$

$$
\times \left(\frac{(\widehat{\rho}\,c_{\mathrm{p}})_{\mathrm{pen\_hnf}}}{(\widehat{\rho}\,c_{\mathrm{p}})_f} \right) \mathrm{Ec} \left\{ \left(\frac{\widehat{u}_{i,j+1}^{(n+1/2)} - \widehat{u}_{i,j-1}^{(n+1/2)}}{2k} + \frac{\widehat{v}_{i+1,j}^{(n+1/2)} - \widehat{v}_{i-1,j}^{(n+1/2)}}{2h} \right)^2 + 4 \left(\frac{\widehat{u}_{i+1,j}^{(n+1/2)} - \widehat{u}_{i-1,j}^{(n+1/2)}}{2h} \right)^2 \right\},
$$

$$
\frac{\tilde{\psi}_{i-1,j}^{(n+1)} + \tilde{\psi}_{i+1,j}^{(n+1)} - 2\tilde{\psi}_{i,j}^{(n+1)}}{h^2} + \frac{\tilde{\psi}_{i,j-1}^{(n+1)} + \tilde{\psi}_{i,j+1}^{(n+1)} - 2\tilde{\psi}_{i,j}^{(n+1)}}{k^2} = -\widehat{w}_{i,j}^{(n+1/2)}, \tag{17}
$$

$$
\widehat{u}_{i,j}^{(n+1)} = \frac{-\tilde{\psi}_{i,j-1}^{(n+1)} + \tilde{\psi}_{i,j+1}^{(n+1)}}{2k}, \quad \widehat{v}_{i,j}^{(n+1)} = -\frac{\tilde{\psi}_{i+1,j}^{(n+1)} - \tilde{\psi}_{i-1,j}^{(n+1)}}{2h}, \tag{18}
$$

$$
\frac{\widehat{w}_{i,j}^{(n+1)} - \widehat{w}_{i,j}^{(n+1/2)}}{\delta t/2} = \frac{1}{\mathrm{Re}} \left(\frac{\mu_{\mathrm{pen\_hnf}}}{\mu_f} \right) (\widehat{\rho}_f/\widehat{\rho}_{\mathrm{pen\_hnf}}) \left\{ \frac{\widehat{w}_{i-1,j}^{(n+1/2)} - 2\widehat{w}_{i,j}^{(n+1/2)} + \widehat{w}_{i+1,j}^{(n+1/2)}}{h^2} + \frac{\widehat{w}_{i,j-1}^{(n+1)} - 2\widehat{w}_{i,j}^{(n+1)} + \widehat{w}_{i,j+1}^{(n+1)}}{k^2} \right\}
$$

$$
+ \frac{\mathrm{Mn}}{(\widehat{\rho}_{\mathrm{pen\_hnf}}/\widehat{\rho}_f)} H_{i,j} \left[\frac{H_{i,j+1} - H_{i,j-1}}{2k} \frac{\widehat{\theta}_{i+1,j}^{(n+1)} - \widehat{\theta}_{i-1,j}^{(n+1)}}{2h} - \frac{H_{i+1,j} - H_{i-1,j}}{2h} \frac{\widehat{\theta}_{i,j+1}^{(n+1)} - \widehat{\theta}_{i,j-1}^{(n+1)}}{2k} \right] \tag{19}
$$

$$
- \widehat{u}_{i,j}^{(n+1/2)} \left(\frac{\widehat{w}_{i+1,j}^{(n+1)} - \widehat{w}_{i-1,j}^{(n+1)}}{2h} \right) - \widehat{v}_{i,j}^{(n+1/2)} \left(\frac{\widehat{w}_{i,j+1}^{(n+1)} - \widehat{w}_{i,j-1}^{(n+1)}}{2k} \right),
$$

$$\frac{\widehat{\theta}_{i,j}^{(n+1)} - \widehat{\theta}_{i,j}^{((n+1/2))}}{\delta t/2} = \left\{ \frac{\widehat{\theta}_{i-1,j}^{(n+1/2)} - 2\widehat{\theta}_{i,j}^{(n+1/2)} + \widehat{\theta}_{i+1,j}^{(n+1/2)}}{h^2} + \frac{\widehat{\theta}_{i,j-1}^{(n+1)} + \widehat{\theta}_{i,j+1}^{(n+1)} - 2\widehat{\theta}_{i,j}^{(n+1)}}{k^2} \right\} + \mathrm{Pr} \times \left(\frac{\mu_{\mathrm{f}}}{\mu_{\mathrm{pen\_hnf}}} \right) (\widehat{\rho_{\mathrm{pen\_hnf}}}/\widehat{\rho_{\mathrm{f}}})$$

$$\times (\widehat{\rho_{\mathrm{pen\_hnf}}}/\widehat{\rho_{\mathrm{f}}}) \times \frac{\mathrm{Mn}}{(\widehat{\rho_{\mathrm{pen\_hnf}}}/\widehat{\rho_{\mathrm{f}}})} \mathrm{Re} \times \left(\frac{1}{(\widehat{\rho_{\mathrm{pen\_hnf}}}/\widehat{\rho_{\mathrm{f}}}) \left(\frac{\mu_{\mathrm{f}}}{\mu_{\mathrm{pen\_hnf}}} \right)} \right) H_{i,j}(\tilde{\psi}_{i,j} - \varepsilon) \left\{ \widehat{u}_{i,j}^{(n+1/2)} \frac{H_{i,j+1} - H_{i,j-1}}{2k} \right.$$

$$\left. + \widehat{v}_{i,j}^{(n+1/2)} \frac{H_{i+1,j} - H_{i-1,j}}{2h} \right\} - \widehat{u}_{i,j}^{(n+1/2)} \left(\frac{\widehat{\theta}_{i+1,j}^{(n+1/2)} - \widehat{\theta}_{i-1,j}^{(n+1/2)}}{2h} \right) - \widehat{v}_{i,j}^{(n+1/2)} \left(\frac{\widehat{\theta}_{i,j+1}^{(n+1)} - \widehat{\theta}_{i,j-1}^{(n+1)}}{2k} \right) \qquad . \quad (20)$$

$$- \mathrm{Pr} \times \left(\frac{\mu_f}{\mu_{\mathrm{pen\_hnf}}} \right) (\widehat{\rho_{\mathrm{pen\_hnf}}}/\widehat{\rho_{\mathrm{f}}}) \times \left(\frac{(\widehat{\rho} \, c_{\mathrm{p}})_{\mathrm{pen\_hnf}}}{(\widehat{\rho} \, c_{\mathrm{p}})_{\mathrm{f}}} \right) \mathrm{Ec} \left\{ \left(\frac{\widehat{u}_{i,j+1}^{(n+1/2)} - \widehat{u}_{i,j-1}^{(n+1/2)}}{2k} + \frac{\widehat{v}_{i+1,j}^{(n+1/2)} - \widehat{v}_{i-1,j}^{(n+1/2)}}{2h} \right)^2 \right.$$

$$\left. + 4 \left(\frac{\widehat{u}_{i+1,j}^{(n+1/2)} - \widehat{u}_{i-1,j}^{(n+1/2)}}{2h} \right)^2 \right\} \right\}$$

The iteration process halts when the following criterion is met

$$\max\{\mathrm{abs}(\tilde{\psi}_{i,j}^{(n+1)} - \tilde{\psi}_{i,j}^{(n)}), \mathrm{abs}(w_{i,j}^{(n+1)} - w_{i,j}^{(n)}), \mathrm{abs}(\theta_{i,j}^{(n+1)}$$
$$- \theta_{i,j}^{(n)})\} < \mathrm{TOL},$$

indicating the attainment of a steady-state solution. In this study, we establish a threshold of TOL $< 10^{-6}$.

4.1 Flowchart illustrating our computational methodology

Illustrated in Figure 2 is the numerical model employed for the ADI scheme.

4.2 Benchmarking the numerical scheme

To verify the reliability and accuracy of our numerical approach, we undertake a rigorous validation process. We use the esteemed work of Yasmin *et al.* [41] as our benchmark for comparison, providing a solid reference point. Our focus lies on the horizontal velocity profiles, which distinctly reveal oscillations in the horizontal component of fluid velocity along a vertical axis. In our investigation, we explore a notable limiting scenario where several influential factors are set to zero: i.e., $(\widehat{\varphi}_1 = \widehat{\varphi}_2 = 0, \mathrm{Mn} = 0)$. In this intriguing domain, the fluid's motion is driven by the motion of horizontal lids in opposite directions. Our analysis is conducted along three different horizontal lines strategically positioned at $y = 0.25$, 0.50, and 0.75, where y represents the vertical coordinates, carefully normalized by the height of the lid-driven cavity, as depicted in the informative Figure 3a. The horizontal velocity along the cross-section defined by $x = 0.25$, 0.50, and 0.75 is presented in Figure 3b, utilizing both our current approach and the findings of Yasmin *et al.* [41]. It is evident that an exact comparison validates our technique.

In order to confirm the accuracy of our code, we compared our results with those from previous studies on natural convection within an enclosure. This problem has been previously investigated by Chen *et al.* [42] and Davis [43], who employed the finite-difference method and the lattice Boltzmann method, respectively. The numerical analysis presented in Table 2 demonstrates a close agreement with the Nu values reported in these earlier studies, validating the reliability of our approach.

In this study, we utilize water as the base fluid, augmented with a blend of nanoparticles comprising Ag, SWCNT, TiO_2, Cu, and Fe_3O_4. These nanoparticles are ingeniously incorporated into the base fluid to enhance thermal conduction and facilitate heat transfer improvement. In our simulations, we set the value of $\varepsilon = 0.02$ to represent the thermophysical properties of this exceptional penta-hybrid nanofluid.

To provide a framework for our research, we introduce two significant dimensionless parameters:
• The Reynolds number serves as a crucial indicator of the balance between inertial and viscous forces in fluid flow.
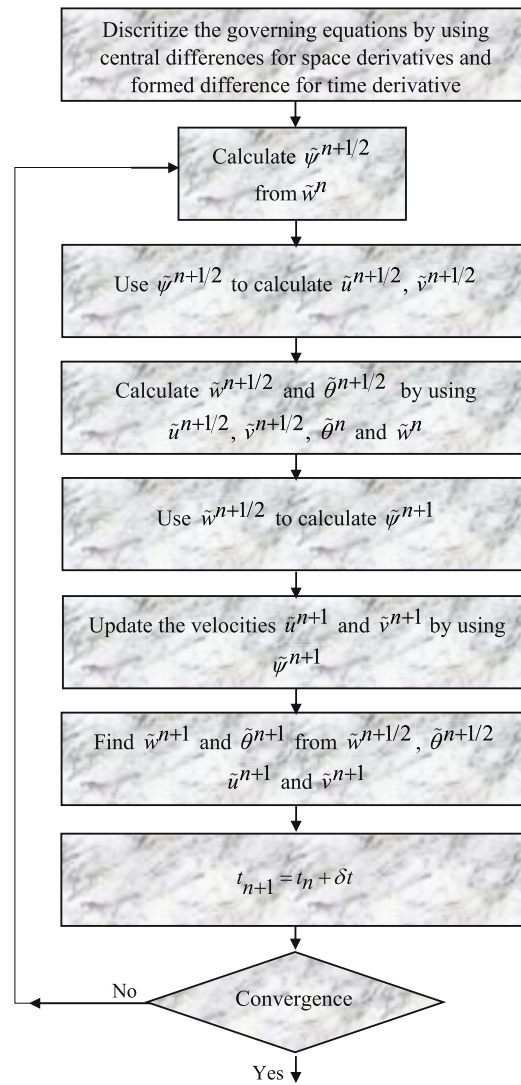
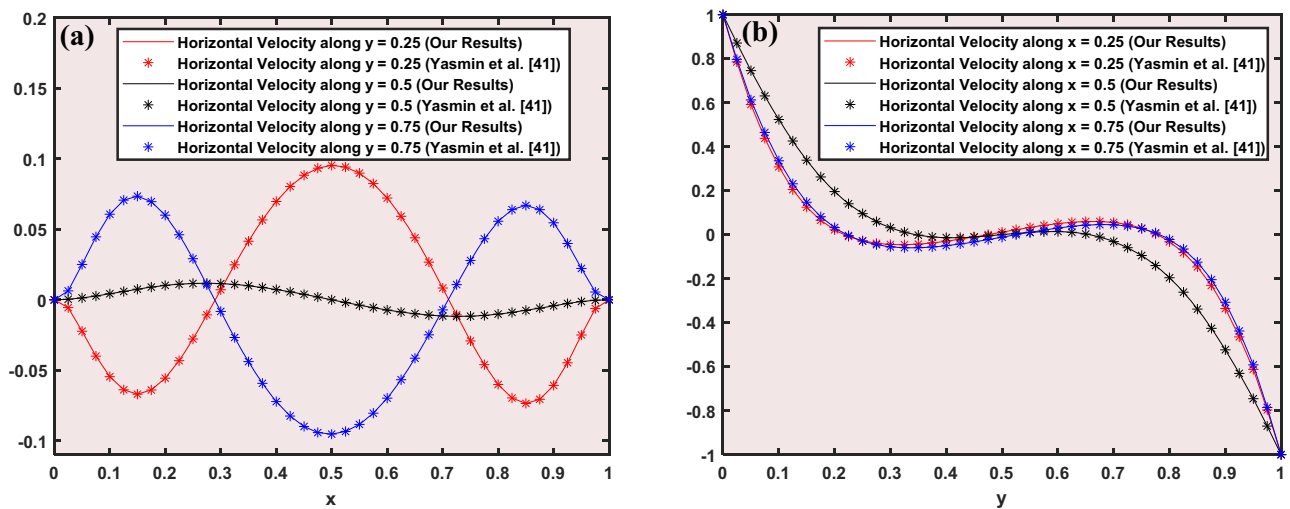**Figure 2:** A flow chart of the pseudo-transient approach.

Figure 3: Numerical results in regard to Yasmin *et al.*'s analytical solution [41].

Table 2: Evaluating our results against previous research: quality assessment

Re	Average Nu for the hot wall lattice Boltzmann's approach (Table 2 in [42])	Finite-difference approach (Tables 1, 2 in [43])	Our approach
10^3	1.1192	1.1181	1.1182
10^4	2.2531	2.2432	2.2481

Table 3: Thermophysical analysis of Ag–SWCNT–TiO$_2$–Cu–Fe$_3$O$_4$–water-based nanofluids

	C_p (J kg^{-1}K^{-1})	β (K^{-1})	$\hat{\rho}$ (kg m^{-3})	σ (S × m^{-1})	k(Wm^{-1} K^{-1})
Silver (Ag)	235	1.89×10^{-5}	10.5	3.6×10^7	429
SWCNT	425	0.85×10^{-5}	2,600	1×10^6	6,600
Titanium oxide (TiO$_2$)	670	1.3	5,200	25,000	6
Copper (Cu)	385	1.67×10^{-5}	8,933	5.96×10^7	401
Iron(II,III) oxide (Fe$_3$O$_4$)	670	20.6	5,180	0.112×10^6	80.4
Water	4,179	21×10^{-5}	997.1	5.5×10^{-6}	0.613

- The Eckert number is a dimensionless parameter that elucidates the relationship between kinetic energy and enthalpy change in fluid flow.

When the Reynolds number is exceedingly small, it yields a very low Eckert number (*e.g.*, 10^{-5}), indicating the dominance of viscous forces while kinetic energy becomes negligible. For a comprehensive understanding, Table 3 presents a detailed overview of the fundamental properties of both nanoparticles and the base fluid utilized in our study. These properties encompass particle size, thermal conductivity, specific heat, viscosity, and density, elucidating the groundwork upon which our investigation is built.

Alternatively, in Figure 4, we observe how our computational outcomes progress with the step size, which represents the spacing between adjacent grid points. As the step size decreases, our computational results show smooth convergence. This convergence provides strong evidence of the stability of our numerical methodology, ensuring the absence of unwanted oscillations or divergent outcomes. Moreover, it highlights the robustness of our findings against changes in grid size, *i.e.*, the total number of grid points used for domain discretization. Essentially, this suggests that beyond a certain threshold, increasing the grid size has minimal impact on our results, which further reinforces the credibility of our approach.
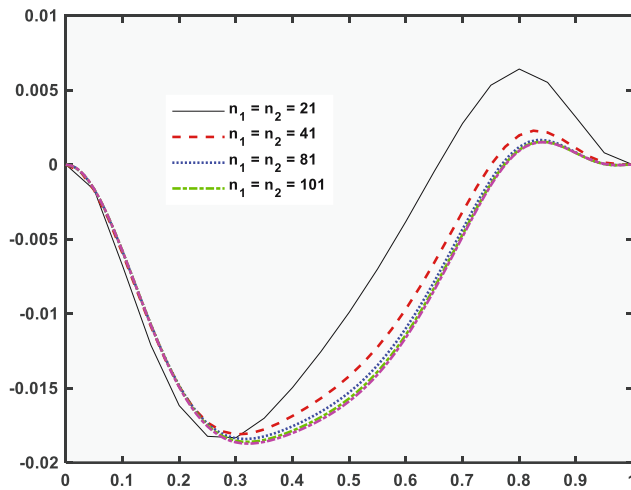
Figure 4: Evaluating grid independence for normal velocity distribution along the line $y = 0.5$.

5 Results and discussion

In this section, we present and analyze visualizations of streamlines and isotherms depicted in tables and figures. These graphical representations offer a comprehensive understanding of temperature dispersion and fluid flow within a cavity. To further interpret our numerical results, corresponding surfaces such as streamlines and temperature distributions are constructed.

The tables provide data on CfRe and Nu at both the top and bottom horizontal walls. CfRe reflects the shear stress exerted by the liquid on the wall, while Nu quantifies the rate of heat transfer through the wall. These results are

relevant to a scenario where the lower and upper horizontal lids of the vertical enclosure move in opposite directions, generating shear-driven flow inside the enclosure.

However, the magnetic field within the enclosure is configured in the form of strips, defined as $\xi_1 \leq \xi \leq \xi_2$; $0 \leq \eta \leq 10$, $\eta_1 \leq \eta \leq \eta_2$; $0 \leq \xi \leq 1$, creating regions with nearly uniform magnetic fields at specific sections of a vertical cavity. This investigation explores several parameters and their respective ranges, including the concentration of nanoparticles ($0 \leq \widehat{\varphi_1}, \widehat{\varphi_2}, \widehat{\varphi_3}, \widehat{\varphi_4}, \widehat{\varphi_5} \leq 0.20$), Reynolds number ($1 \leq Re \leq 25$), magnetized strip length parameter ($0 \leq L \leq 0.4$), and magnetic number ($0 \leq Mn \leq 1,500$), representing the intensity of the magnetic field in the flow. Unless otherwise specified, the default values used are Mn = 5 and Re = 5. Additionally, the flow pattern is influenced by confined magnetic strips, comprising one flat and one vertical strip, as stated earlier.

5.1 Outcomes of the magnetizing force

Figure 5 depicts the influence of magnetic field strength, where vertical and horizontal strips are defined in regions ($0.4 - L < \xi < 0.6 + L$; $0 < \eta < 10$) and ($6.4 - L < \eta < 6.6 + L$; $0 < \xi < 1$), respectively. These strips affect streamlines, isotherms, stress factors, and temperature gradients in the flow regime. The rotation of vortices depends on the

movement of the lower and upper lids of the vertical cavity, driven by an external mechanical setup. Visualizations reveal that both flow patterns and stress factor contours are significantly influenced by the magnetic number Mn. In the absence of a magnetic field, the flow is relatively straightforward, and stress factor contours are evenly distributed. However, as the magnetic number increases, the flow becomes more intricate, and stress factor contours become more irregular. This occurs because the magnetic field exerts a force on fluids, causing them to circulate along field lines. Stronger magnetic fields have a greater impact on motion, resulting in more complex flow patterns. Furthermore, regions with flow exhibit higher levels of stress factors because fluids need to deform to navigate around field lines. These findings suggest that magnetic fields can manipulate both the dynamics and thermal characteristics of fluids. At certain values of magnetic numbers, complex flow patterns give rise to vortex formations, swirling areas within fluids capable of transporting heat and momentum. The irregular spacing of isotherms and uneven contours of temperature gradients, caused by vortices, may find applications in processes and equipment such as cell separation, drug delivery, or magnetic resonance imaging.

In Figure 6, it is noticeable that the isotherms are closer together near the cavity's lids, where the lower horizontal wall is heated, and the upper horizontal wall is cooled. When the magnetic number is low, the isotherms
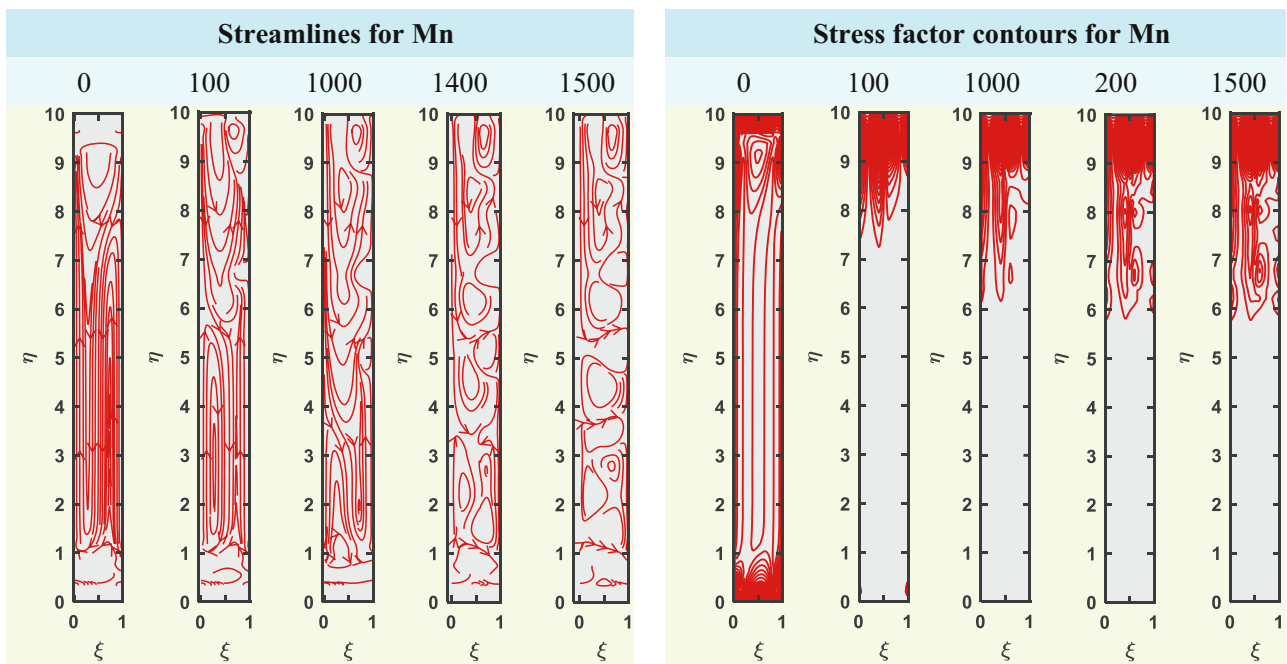

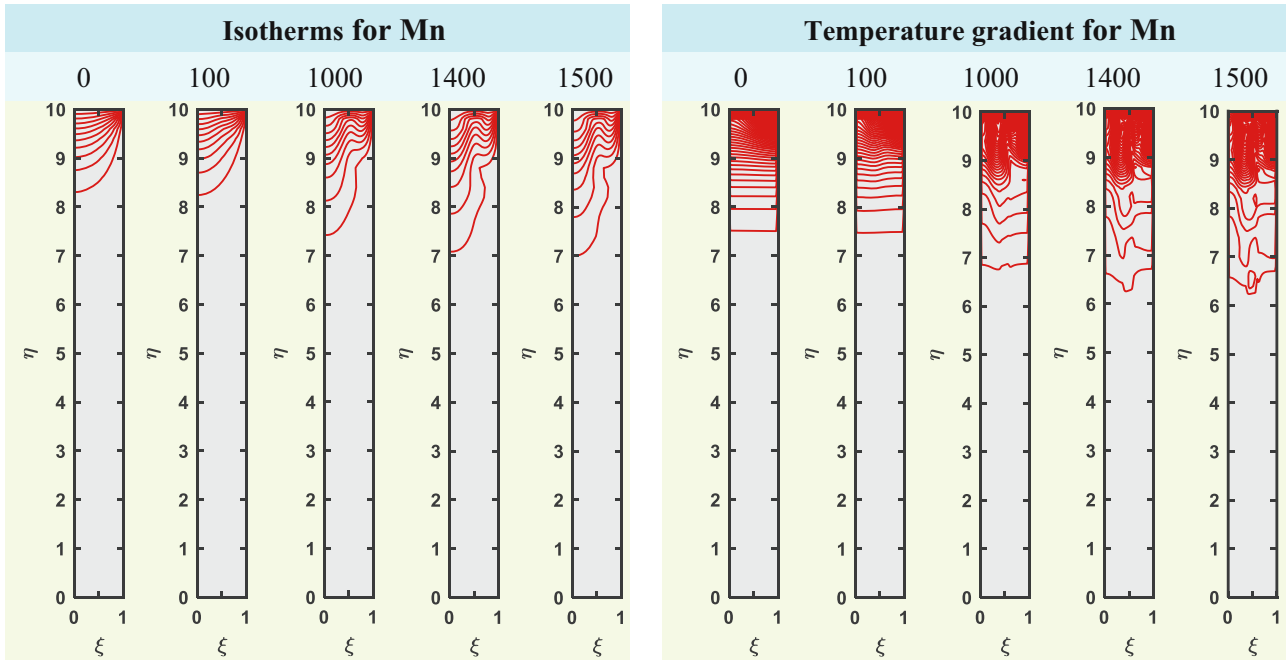**Figure 5:** Streamlines, stress factor contours for the flow with different Mn for Re = 1, Pr = 6.8.

Figure 6: Isotherms, temperature gradient contours for the flow with different Mn for Re = 1, Pr = 6.8.

are evenly spaced, and the temperature gradient contours appear smooth. This implies that the temperature of the fluid remains relatively uniform throughout the cavity. However, as we increase the magnetic number from Mn = 100 to Mn = 1,500, we observe that the spacing between isotherms becomes more irregular, and the temperature

gradient contours appear uniform. This suggests a decrease in temperature uniformity within the fluid across the vertical cavity.

The use of magnetic fields that vary in space when studying the flow of penta-hybrid nanofluid in a lid-driven cavity is very important from a physical perspective. These
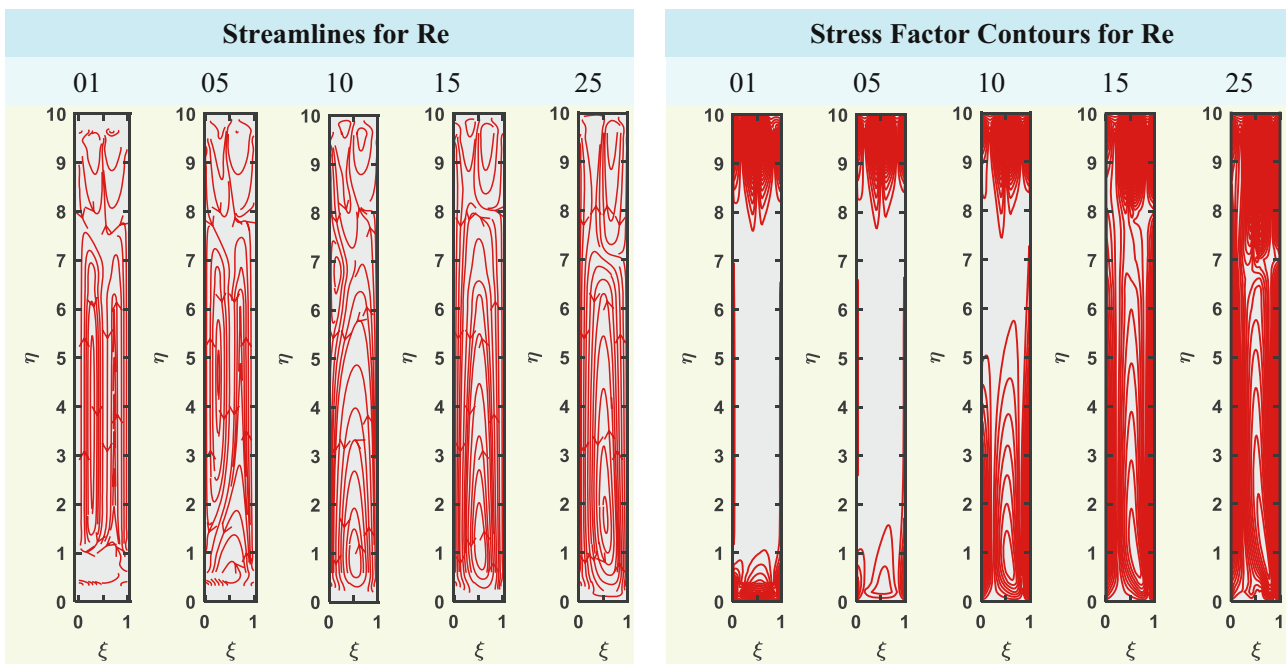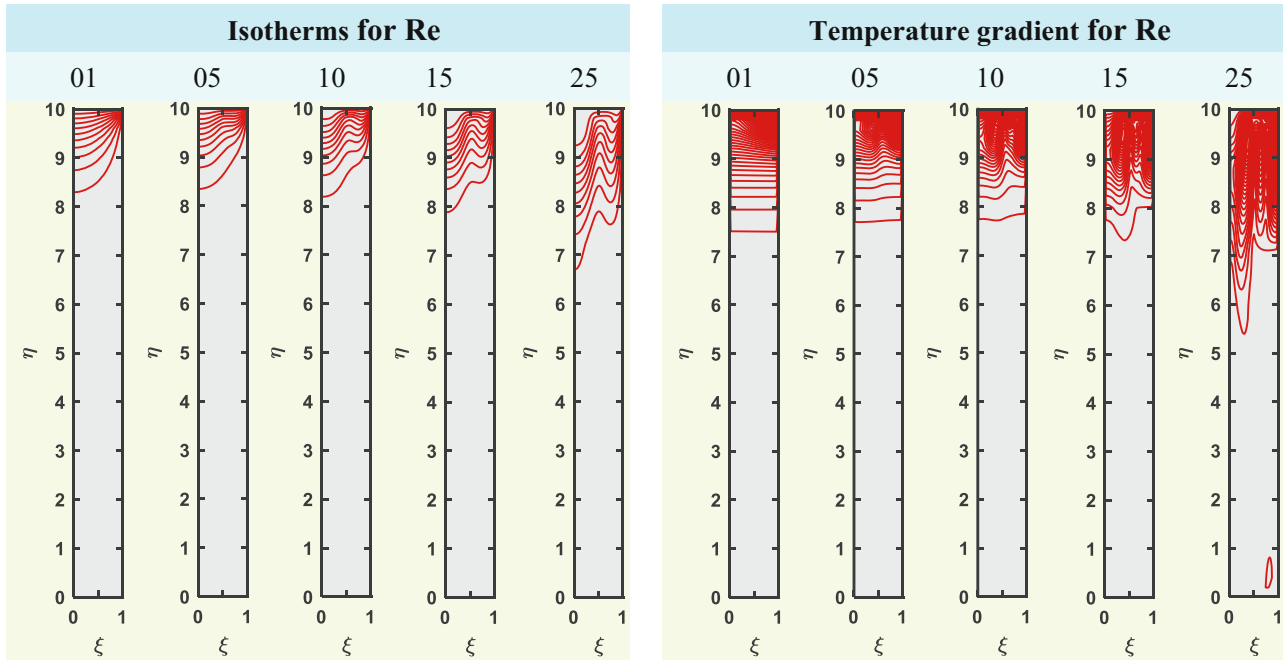

Figure 7: Streamlines and stress factor contours for the flow with different Re for Mn = 10, Pr = 6.8, and L = 0.00.

Figure 8: Isotherms and temperature gradient contours for the flow with different Re for Mn = 10, Pr = 6.8, and *L* = 0.00.

fields can come from different sources like permanent magnets or electromagnets, and their spatial variations create changes in the magnetic flux density across the cavity. This variation in space affects how the nanofluid behaves, influencing its flow patterns, heat transfer properties, and overall fluid dynamics. Understanding the physical importance of spatially varying magnetic fields helps us better represent real-world situations where magnetic fields are not uniform. By studying how these varying magnetic fields interact with the complex behavior of penta-hybrid nanofluids, researchers can gain valuable insights into the dynamics of magnetic fluid systems. This research contributes to advancements in various fields, such as engineering, materials science, and biomedical applications. Therefore, exploring the physical significance of spatially varying magnetic fields is essential for understanding how magnetic forces and fluid flow phenomena interact within lid-driven cavities.

5.2 Impact of the Reynolds number

In Figure 7, we observe the flow patterns and stress distribution at different Reynolds numbers (Re), maintaining Mn = 10, Pr = 6.8, and *L* = 0.000 as constants. As the Reynolds number rises, the flow patterns become more complex and disorderly. This behavior is linked to the

impact of higher Reynolds numbers, which may trigger turbulence by boosting inertial forces. The stress distribution shows that stress levels are most pronounced near the walls and in areas with high velocity. This correlation arises because shear stress is particularly pronounced in these areas.

As depicted in Figure 8, the Reynolds number seems to influence the distribution of temperature in flows with fields. When the Reynolds number is low, the temperature distribution remains uniform, with most of the temperature gradient concentrated in the flow region. As the Reynolds number increases, the temperature distribution becomes more intricate and uneven across the domain. Therefore, accurately predicting temperature distributions requires considering how the Reynolds number affects the temperature field.

When studying how spatially varying magnetic fields impact penta-hybrid nanofluid flow in a lid-driven cavity, understanding the physical significance of the Reynolds number is essential. In this specific scenario, the Reynolds number acts as a key indicator of flow behavior. Examining the Reynolds number helps distinguish between laminar and turbulent states, offering insights into how stable and predictable nanofluid flow is within the cavity under different magnetic field conditions. Additionally, analyzing the effects of both Reynolds number and magnetic field variations provides a comprehensive view of how fluid flow dynamics are influenced by viscous and magnetic forces,
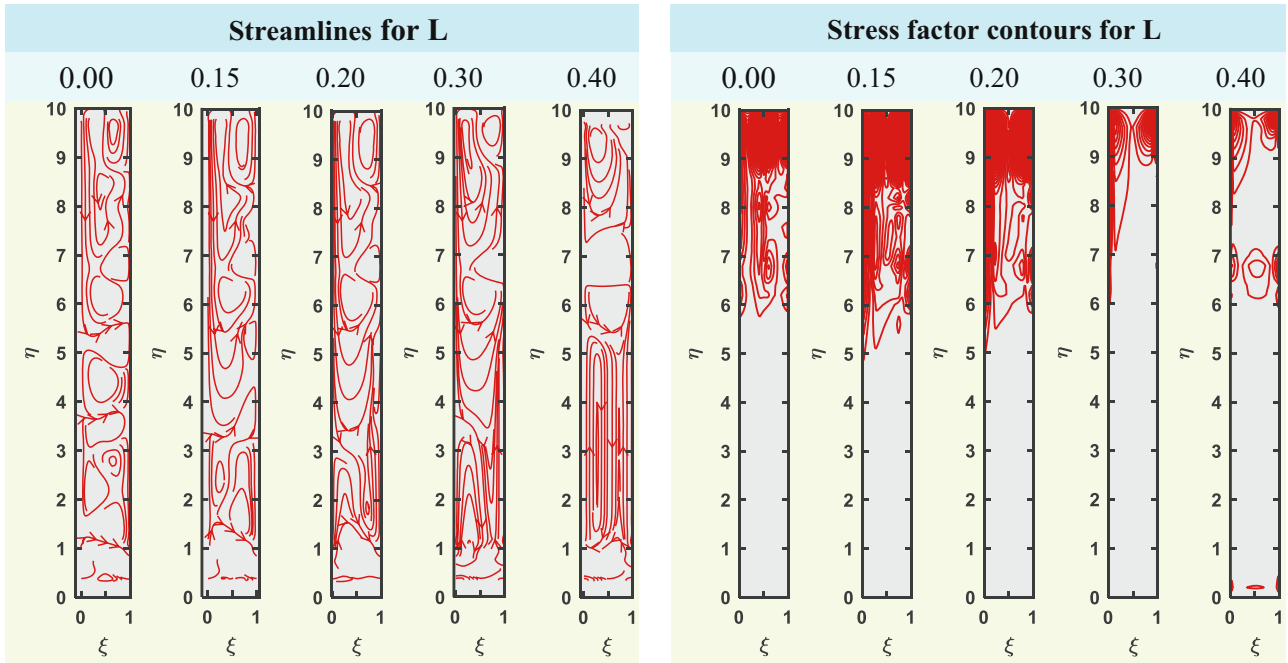
Figure 9: Streamlines and stress factor contours for the flow with different L for Mn = 1,500, Re = 1, and Pr = 6.8.

shedding light on how these parameters interact intricately. In engineering applications such as heat exchangers or combustion chambers, having knowledge of this temperature distribution is crucial as it directly impacts processes like heat transfer efficiency or engine performance in terms of oil input and kinetic output.

5.3 Impact of magnetic field localization

To investigate the role of magnetic field width, we define strips within the flow field using parameters ($0.4 - L < \xi < 0.6 + L$, $0 < \eta < 10$) and ($6.4 - L < \eta < 6.6 + L$; $0 < \xi < 1$). The parameter L determines the width of these strips, where
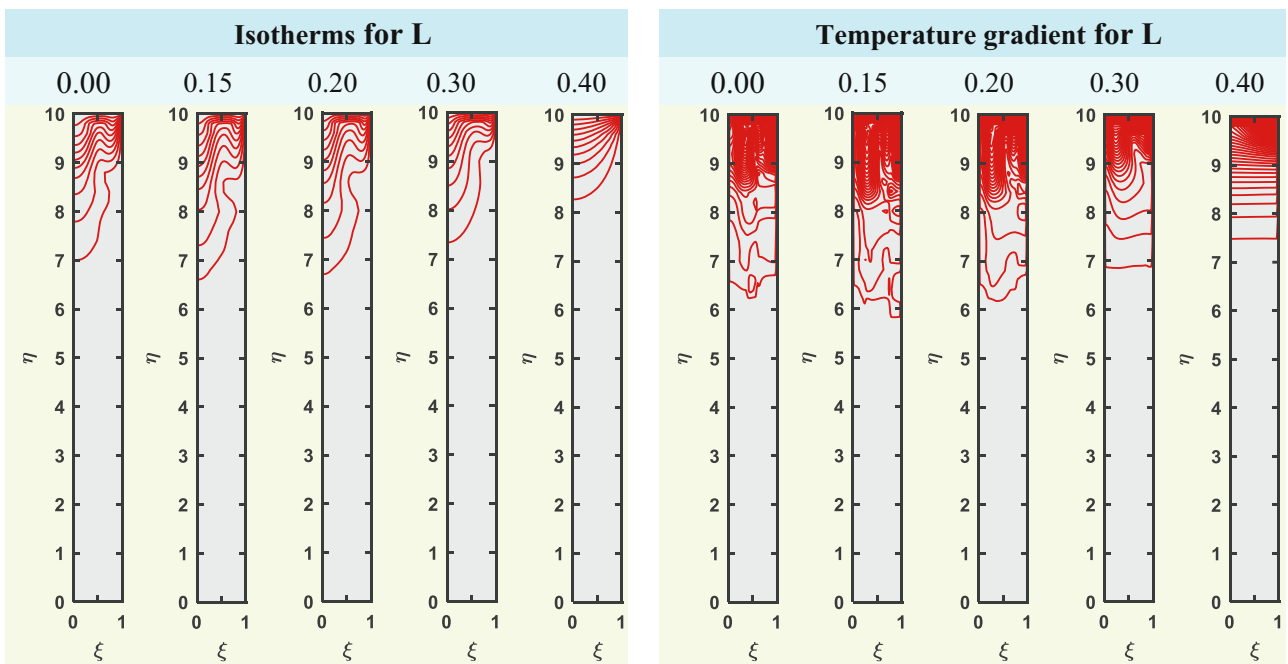

Figure 10: Isotherms and temperature gradient for the flow with different L for Mn = 1,500, Re = 1, and Pr = 6.8.

L = 0.4 indicates that the magnetic field occupies nearly the entire cavity, while L = 0.0 suggests that the magnetic field is confined to the strips ($0.4 < \xi < 0.6$; $0 < \eta < 10$ and $6.4 < \eta < 6.6$; $0 < \xi < 1$). Interestingly, when the magnetic field occupies the entire flow field, significant impacts on the flow and temperature distributions are not observed. However, as shown in Figures 9 and 10, confining the magnetic field intensity within strips results in the emergence of new vortices while eliminating the primary ones. In contrast, the isotherms exhibit a zig-zag pattern, indicating vigorous mixing of fluid layers at different temperatures.

5.4 The effects of Mn, Re, and magnetized strips on heat transfer and fluid flow

Heat transfer and skin friction are crucial factors in the design of various devices, including heat exchangers, air conditioners, and electronic cooling systems. Two key parameters influencing heat transfer and fluid flow are the Nu and the CfRe. The Nu characterizes the convective to conductive heat transfer ratio at a boundary within a fluid, with a higher Nu indicating a greater rate of heat transfer. On the other hand, CfRe assesses the resistance of fluid flow against the wall, where a higher CfRe indicates an increase in pressure. The impact of magnetic field strength (Mn) and Reynolds number (Re) on Nu and CfRe can be summarized as follows (refer to Tables 4 and 5):

- Increasing Mn results in a significant decrease in Nu and a slight rise in CfRe. This implies that a stronger magnetic field reduces heat transfer while boosting pressure. This is because the magnetic field hinders microrotation, where fluid particles spin around their axes.
- With increasing Re, Nu fluctuates while CfRe drops. Several factors contribute to this. As Re rises, the flow becomes more turbulent, strengthening the main vortex while weakening secondary ones. This enhances fluid mixing, boosting heat transfer efficiency and leading to

Table 5: The influence of Reynolds numbers on Nu and CfRe for Re = 1 and Mn = 5

Re	|Nu|	|CfRe|
01	0.01480	339.5688
5	0.0028	338.0201
10	0.0018	330.1549
15	0.0021	321.4035
25	0.2397	311.2008

higher Nu values. However, fluctuations in the effect of Re on Nu may occur due to intricate interactions among flow dynamics, heat transfer processes, and the magnetic field.

- As Re increases, skin friction decreases as viscous forces become less dominant compared to inertial forces. The magnetic field also impacts skin friction by restraining flow near walls and reducing shear stress. The impact is more noticeable on walls in motion compared to walls that are still.

These effects hold significant implications for device design and optimization. Manipulating Mn, Re, or L allows control over heat transfer rate and pressure drop in various applications. For instance, magnetic fields can enhance heat exchanger performance in air conditioning and refrigeration systems. Nanoparticles, conversely, can augment microrotation, reducing heat transfer and pressure drop in electronic cooling systems.

The parameter L represents a geometric dimension within the rectangular domain where the magnetic field is confined. Table 6 shows the sensitivity of the Nu and skin friction to the expansion of the magnetic field across a broader domain. It shows a significant 4.6% increase in Nu, while the CfRe experiences only a negligible impact from the confined magnetic field. This indicates that Nu is more dependent on the confinement of the magnetic field compared to CfRe.

Table 4: The influence of magnetic numbers on Nu and CfRe for Re = 1 and Mn = 5

Mn	|Nu|	|CfRe|
00	0.0150	339.5719
100	0.0043	339.5555
200	0.0033	339.5721
300	0.0031	339.6023
500	0.0031	339.7011

Table 6: The Influence of strip width (*L*) on Nu and CfRe for Re = 1 and Mn = 1,000

L	|Nu|	|CfRe|
0	0.0036	340.1804
1	0.0061	340.1292
2	0.0072	340.0792
3	0.0113	339.8633
5	0.0202	339.5643

Table 7: Influence of silver particles on Nu and CfRe for Re = 1 and Mn = 50

$\widehat{\varphi}_1$ (Silver)	|Nu|	|CfRe|
0.00	0.0061	362.9440
0.05	0.0062	339.5542
0.10	0.0065	330.2323
0.15	0.0070	331.1494
0.20	0.0076	340.7844

**Table 10:** Influence of copper particles on Nu and CfRe for Re = 1 and Mn = 50

$\widehat{\varphi}_4$ (Copper)	|Nu|	|CfRe|
0.00	0.0060	354.7106
0.05	0.0062	339.5542
0.10	0.0066	335.6801
0.15	0.0071	340.7637
0.20	0.0078	354.0348

Table 8: Influence of SWCNT on Nu and CfRe for Re = 1 and Mn = 50

$\widehat{\varphi}_2$ (SWCNT)	|Nu|	|CfRe|
0.00	0.0057	305.4432
0.05	0.0062	339.5542
0.10	0.0068	380.2868
0.15	0.0075	429.4104
0.20	0.0083	489.3182

Table 11: Influence of iron(II,III) oxide particles on Nu and CfRe for Re = 1 and Mn = 50

$\widehat{\varphi}_5$ (Iron(II,III) oxide)	|Nu|	|CfRe|
0.00	0.0058	321.8965
0.05	0.0062	339.5542
0.10	0.0067	362.5569
0.15	0.0074	391.8928
0.20	0.0081	428.9914

5.5 How different nanoparticles affect heat transfer and fluid flow

Tables 7–11 explore the effects of five types of nanoparticles – silver, single-walled carbon nanotubes (SWNTs), titanium dioxide, copper, and iron oxide, respectively. Introducing nanoparticles into the fluid enables them to absorb heat from the fluid, transferring it to the channel walls. This increases the temperature difference between the fluid and walls, thereby elevating Nu. Increasing the concentration of these nanoparticles results in higher Nus.

The addition of nanoparticles to the fluid can impact CfRe differently. Silver nanoparticles induce turbulence in the fluid, reducing CfRe by decreasing the velocity gradient near the wall. Similarly, SWCNTs form a network that acts as a barrier to flow, also leading to a reduction in CfRe by lowering the velocity gradient near the wall. Conversely, titanium dioxide nanoparticles possess abrasiveness, which smoothers the enclosure's surface and increases CfRe. Iron

Table 9: Influence of titanium dioxide particles on Nu and CfRe for Re = 1 and Mn = 50

$\widehat{\varphi}_3$ (Titanium dioxide)	|Nu|	|CfRe|
0.00	0.0052	316.4691
0.05	0.0062	339.5542
0.10	0.0076	368.0199
0.15	0.0093	403.1068
0.20	0.0115	446.5200

oxide and copper nanoparticles can form a protective layer on the cavity's surface, reducing CfRe by smoothing the geometry's surface (Tables 7–11).

Overall, adding nanoparticles to the fluid can increase Nu while also increasing CfRe, enhancing both heat transfer and skin friction. This improves the performance of devices involving heat transfer and fluid flow. However, it is crucial to note that different types of nanoparticles have varying effects on Nu and CfRe based on properties such as conductivity, surface area, and their ability to promote turbulence. Among these nanoparticles, titanium dioxide stands out due
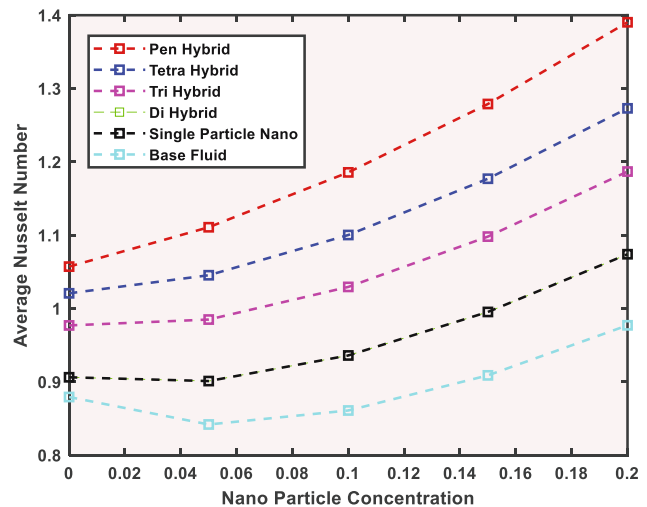
Figure 11: Assessing hybrid nanofluid in comparison to the penta-hybrid nanoparticles for Mn = 150, Re = 1, and *L* = 0.00.

to its influence on Nu and its moderate effect on CfRe, making it an exciting material for applications where efficient heat transfer is critical.

5.6 Comparative analysis of nanomaterial thermal characteristics

Figure 11 depicts that penta-hybrid fluids showcase enhanced heat transfer performance, as indicated by their notably higher average Nu in comparison to nano/hybrid or tetra-hybrid nanofluids.

5.7 Importance of magnetic field strength

Figure 12 depicts the impact of parameters A1 and A2, which control the intensity of the magnetic field, on the average Nu. The Nu shows greater dependency on A1 and A2 when their values are lower. Significant variations were observed in our numerical findings when assigning A1 and A2 to 50 and 100. Therefore, for this study, we selected A1 = A2 = 50 unless specified otherwise.

5.8 Significance of confined magnetic field

The magnetic strips can be defined as follows: $(0.4 - L < \xi < 0.6 + L, 0 < \eta < 10)$ and $(6.4 - L < \eta < 6.6 + L; 0 < \xi < 1)$. This
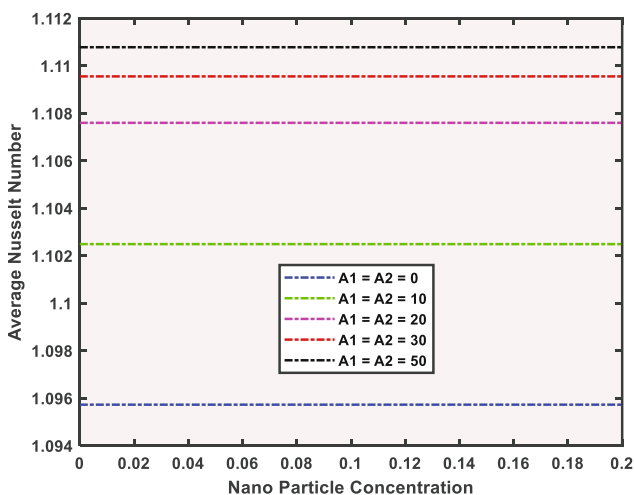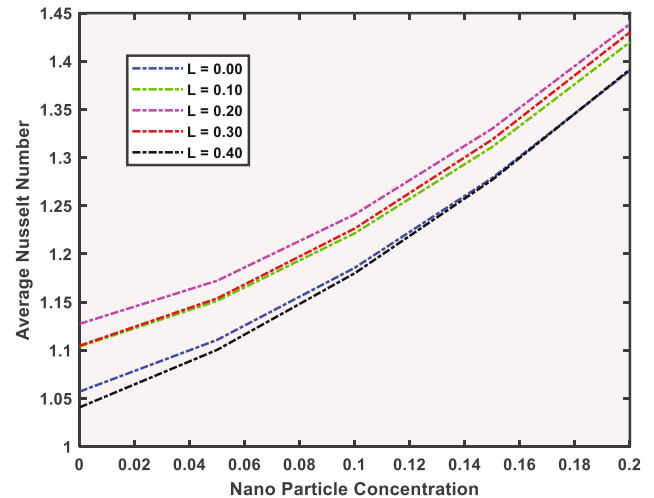
Figure 13: The impact of magnetic strip dimensions on the average Nu.

indicates that the strips maintain a constant width of 0.2 units when L is zero. Interestingly, the nanostructure influences the Nu differently as the parameter L increases, suggesting a broader strip, as depicted in Figure 13.

6 Concluding remarks

This study delves into the numerical investigation of the interaction between penta-hybrid flow in an enclosed space and an imposed magnetic field, generated by a configuration of horizontal and vertical strips. The penta-hybrid nanofluid is analyzed using Eringen's model. Based on the collected data, the following conclusions can be drawn:

1) Magnetic fields possess the capability to influence both the movement of fluids and their temperature characteristics.
2) The swirling motions within the fluid give rise to temperature differences, represented as isotherms, which can be utilized in various processes and equipment.
3) The flows affected by fields, the Reynolds number plays a significant role in determining the distribution of temperature.
4) The magnetic field tends to suppress rotational movements, resulting in a more uniform temperature distribution throughout the flow.
5) Magnetic field strength (Mn) and Reynolds number (Re) impact Nu and CfRe differently.
6) Re enhances Nu and CfRe by increasing flow turbulence and velocity.
7) Different applications necessitate different combinations of Mn, Re, and L to achieve optimal heat transfer and pressure drop.

Figure 12: Influence of parameters A1 and A2 on the average Nu.

8) Incorporating nanoparticles into a fluid can increase the Nu and decrease the CfRe, thereby enhancing heat transfer and reducing pressure drop.

9) Titanium oxide nanoparticles exhibit the most significant effect on Nu and a moderate effect on CfRe, making them promising for applications involving heat exchange or scenarios where efficient heat transfer is crucial.

10) Other types of nanoparticles, such as SWCNT, silver, and copper, also positively impact Nu and CfRe, albeit to a lesser extent compared to titanium dioxide.

Author contributions: All authors have accepted responsibility for the entire content of this manuscript and approved its submission.

Conflict of interest: The authors state no conflict of interest.

Data availability statement: The datasets generated during and/or analyzed during the current study are available from the first author, Shabbir Ahmad, upon reasonable request.

References

[1] Ismael MA, Armaghani T, Chamkha AJ. Mixed convection and entropy generation in a lid-driven cavity filled with a hybrid nanofluid and heated by a triangular solid. Heat Transf Res. 2018;49(17).

[2] Ahlawat A, Chaudhary S, Loganathan K, Sharma MK, Abbas M, Bhavana M. Heat convection and irreversibility of magneto-micropolar hybrid nanofluids within a porous hexagonal-shaped enclosure having heated obstacle. Nanotechnol Rev. 2024;13(1):20240044.

[3] Rehman S, Alqahtani S, Eldin SM, Hashim, Alshehery S. An extended model to assess Jeffery–Hamel blood flow through arteries with iron-oxide (Fe_2O_3) nanoparticles and melting effects: Entropy optimization analysis. Nanotechnol Rev. 2024;13(1):20230160.

[4] Zhang D, Deng P, Hou R, Song Y, Liu J, Zhang W. Study on cavitation and pulsation characteristics of a novel rotor-radial groove hydrodynamic cavitation reactor. Open Phys. 2024;22(1):20240030.

[5] Waseem F, Sohail M, Sarhan N, Awwad EM, Khan MJ. Utilization of OHAM to investigate entropy generation with a temperature-dependent thermal conductivity model in hybrid nanofluid using the radiation phenomenon. Open Phys. 2024;22(1):20240059.

[6] Idris M, Nor Azwadi C, Izual N. Vortex structure in a two dimensional triangular lid-driven cavity. AIP Conference Proceedings. American Institute of Physics; 2012.

[7] Khan MI, Mansir IB, Raza A, Khan SU, Elattar S, Said HM, et al. Fractional simulations for thermal flow of hybrid nanofluid with aluminum oxide and titanium oxide nanoparticles with water and blood base fluids. Nanotechnol Rev. 2022;11(1):2757–67.

[8] Thirumalaisamy K, Ramachandran S, Ramachandra Prasad V, Anwar Bég O, Leung H-H, Kamalov F, et al. Comparative heat transfer analysis of electroconductive Fe3O4–MWCNT–water and Fe3O4–MWCNT–kerosene hybrid nanofluids in a square porous cavity using the non-Fourier heat flux model. Phys Fluids. 2022;34(12).

[9] Akram M, Benhanifia K, Brahim M, Rahmani L, Ansari AZ, Eid MR, et al. Natural convection and flow patterns of Cu–water nanofluids in hexagonal cavity: A novel thermal case study. Open Physics. 2024;22(1):20240041.

[10] Asghar A, Dero S, Lund LA, Shah Z, Alshehri MH, Vrinceanu N. Slip effects on magnetized radiatively hybridized ferrofluid flow with acute magnetic force over shrinking/stretching surface. Open Phys. 2024;22(1):20240052.

[11] Li M-C, Chen A-X, Zeng W. Tripartite entanglement and entanglement transfer in a hybrid cavity magnomechanical system. Open Phys. 2023;21(1):20220240.

[12] Hwang J-J, Chang B-Y. Effect of outflow orientation on heat transfer and pressure drop in a triangular duct with an array of tangential jets. J Heat Transf. 2000;122(4):669–78.

[13] Waqas H, Hasan MJ, Naqvi SMRS, Liu D, Muhammad T, Eldin SM, et al. Enhancing the performance of thermal energy storage by adding nano-particles with paraffin phase change materials. Nanotechnol Rev. 2024;13(1):20230180.

[14] Hayat U, Shaiq S, Nisar KS, Shahzad A, Farooq A, Kamran M, et al. Comparative study of copper nanoparticles over radially stretching sheet with water and silicone oil. Nanotechnol Rev. 2024;13(1):20230200.

[15] Hanif H, Shafie S, Roslan R, Ali A. Collision of hybrid nanomaterials in an upper-convected Maxwell nanofluid: A theoretical approach. J King Saud Univ-Sci. 2023;35(1):102389.

[16] Shahzad MA, Safaei B, Sahmani S, Basingab MS, Hameed AZ. Nonlinear three-dimensional stability characteristics of geometrically imperfect nanoshells under axial compression and surface residual stress. Nanotechnol Rev. 2023;12(1):20220551.

[17] Hanif H. A finite difference method to analyze heat and mass transfer in kerosene based γ-oxide nanofluid for cooling applications. Phys Scr. 2021;96(9):095215.

[18] Lone SA, Al-Essa LA, Al-Bossly A, Alduais FS, Ali F, Eldin SM, et al. Entropy minimization of GO–Ag/KO cross-hybrid nanofluid over a convectively heated surface. Nanotechnol Rev. 2023;12(1):20230101.

[19] Li S, Sohail M, Nazir U, Sherif E-SM, Hassan AM. Statistical investigations and morphological aspects of cross-rheological material suspended in transportation of alumina, silica, titanium, and ethylene glycol via the Galerkin algorithm. Nanotechnol Rev. 2023;12(1):20230169.

[20] Rahman M, Öztop HF, Rahim N, Saidur R, Al-Salem K. MHD mixed convection with joule heating effect in a lid-driven cavity with a heated semi-circular source using the finite element technique. Numer Heat Transfer, Part A: Appl. 2011;60(6):543–60.

[21] Selimefendigil F, Oztop HF, Chamkha AJ. MHD mixed convection and entropy generation of nanofluid filled lid driven cavity under the

influence of inclined magnetic fields imposed to its upper and lower diagonal triangular domains. J Magn Magn Mater. 2016;406:266–81.

[22] Lone SA, Allehiany FM, Anwar S, Shahab S, Saeed A, Eldin SM. Investigating effects of Lorentz forces and convective heating on ternary hybrid nanofluid flow over a curved surface using homotopy analysis method. Nanotechnol Rev. 2023;12(1):20230125.

[23] Żebrowska K, Grabowska M, Coy E, Rolle K, Mrówczyński R, Grześkowiak BF. In vitro anticancer activity of melanin-like nanoparticles for multimodal therapy of glioblastoma. Nanotechnol Rev. 2024;13(1):20230206.

[24] Korei Z, Benissaad S. Entropy generation of a hybrid nanofluid on MHD mixed convection is a lid-driven cavity with partial heating having two rounded corners. E3S Web of Conferences. EDP Sciences; 2021.

[25] Yasmin H, Lone SA, Mahnashi AM, Hamali W, Shamshuddin MD, Saeed A. Optimized framework numerical solution for swirling hybrid nanofluid flow with silver/gold nanoparticles on a stretching cylinder with heat source/sink and reactive agents. Open Phys. 2024;22(1):20230202.

[26] Panda S, Pattnaik PK, Mishra SR, Alkarni S, Shah NA. Improving heat transfer efficiency via optimization and sensitivity assessment in hybrid nanofluid flow with variable magnetism using the Yamada–Ota model. Open Phys. 2024;22(1):20240075.

[27] Hanif H. Cattaneo–Friedrich and Crank–Nicolson analysis of upper-convected Maxwell fluid along a vertical plate. Chaos, Solitons Fractals. 2021;153:111463.

[28] Al-Kouz W, Owhaib W, Souayeh B, Sabir Z. Inclined magnetized infinite shear rate viscosity of non-Newtonian tetra hybrid nanofluid in stenosed artery with non-uniform heat sink/source. Open Phys. 2024;22(1):20240040.

[29] Manna NK, Biswas N. Magnetic force vectors as a new visualization tool for magnetohydrodynamic convection. Int J Therm Sci. 2021;167:107004.

[30] Algehyne EA, Raizah Z, Gul T, Saeed A, Eldin SM, Galal AM. Cu and Al2O3-based hybrid nanofluid flow through a porous cavity. Nanotechnol Rev. 2023;12(1):20220526.

[31] Ali K, Ahmad S, Ahmad S, Tayebi T. Impact of magnetic field localization on the vortex generation in hybrid nanofluid flow. J Therm Anal Calorim. 2023;148:6283–300.

[32] Hussain SM, Ali K, Ahmad S, Qureshi MA, Abd-Elmonem A, Jamshed W, et al. Characterizing magnetohydrodynamic effects on developed nanofluid flow in an obstructed vertical duct under constant pressure gradient. Open Phys. 2024;22(1):20240070.

[33] Talebi F, Mahmoudi AH, Shahi M. Numerical study of mixed convection flows in a square lid-driven cavity utilizing nanofluid. Int Commun Heat Mass Transf. 2010;37(1):79–90.

[34] Batool S, Rasool G, Alshammari N, Khan I, Kaneez H, Hamadneh N. Numerical analysis of heat and mass transfer in micropolar nanofluids flow through lid driven cavity: Finite volume approach. Case Stud Therm Eng. 2022;(37):102233.

[35] Loukopoulos V, Tzirtzilakis E. Biomagnetic channel flow in spatially varying magnetic field. Int J Eng Sci. 2004;42(5–6):571–90.

[36] Ahmad S, Ali K, Ashraf M. MHD flow of Cu-Al$_2$O$_3$/water hybrid nanofluid through a porous media. J Porous Media. 2021;24(7).

[37] Ahmad S, Ali K, Sajid T, Bashir U, Rashid FL, Kumar R, et al. A novel vortex dynamics for micropolar fluid flow in a lid-driven cavity with magnetic field localization–A computational approach. Ain Shams Eng J. 2023;15:102448.

[38] Ahmad S, Ali K, Ayub A, Bashir U, Rashid FL, Aryanfar Y, et al. Localized magnetic fields and their effects on heat transfer enhancement and vortices generation in tri-hybrid nanofluids: A novel investigation. Case Stud Therm Eng. 2023;50:103408.

[39] Hanif H, Shafie S, Jagun ZT. Maximizing thermal efficiency of a cavity using hybrid nanofluid. J Clean Prod. 2024;441:141089.

[40] Ahmad S, Cai J, Ali K. Prediction of new vortices in single-phase nanofluid due to dipole interaction. J Therm Anal Calorim. 2022;147(1):461–75.

[41] Yasmin A, Ali K, Ashraf M. MHD Casson nanofluid flow in a square enclosure with non-uniform heating using the Brinkman model. Eur Phys J Plus. 2021;136(2):1–14.

[42] Chen CL, Chang SC, Chen CK, Chang CK. Lattice Boltzmann simulation for mixed convection of nanofluids in a square enclosure. Appl Math Model. 2015;39(8):2436–51.

[43] Davis GD. Natural-convection of air in a square cavity - a benchmark numerical-solution. Int J Numer Methods Fluids. 1983;3(3):249–64.